High-Fidelity Aeropropulsive Assessment of Distributed Electric Propulsion and Boundary Layer Ingestion for the SUSAN Electrofan

Timothy Chau*, Brandon M. Lowe†, and Leonardo Machado‡
Science & Technology Corporation, Moffett Field, CA, 94035, USA

Joshua L. Anibal§ and Jared C. Duensing¶
NASA Ames Research Center, Moffett Field, CA, 94035, USA

This paper presents a high-fidelity aeropropulsive assessment of the SUSAN Electrofan's distributed electric propulsion (DEP) and boundary layer ingestion (BLI) aft fuselage turbofan technologies. This is achieved through the application of computational tools for aerodynamic and aeropropulsive design and analysis based on the Reynolds-averaged Navier-Stokes (RANS) equations. Representative aircraft models are first developed in 3D for the SUSAN Electrofan concept, a non-DEP variant, and a year 2020 technology level reference aircraft based on the Boeing 737-8. These include airframes developed through the application of RANS-based aerodynamic shape optimization, with the objective of drag minimization at cruise while subject to constant lift and zero pitching moment constraints. Wing propulsors are also included and modeled as free-flying ducted fans. These are developed through RANS-based aeropropulsive shape optimization, with the objective of shaft power minimization while subject to constant net thrust and maximum fan face Mach number constraints. An iterative power balance method is then used to trim each of the decoupled aircraft configurations, providing estimates of relative aerodynamic performance, shaft power, and range efficiency. Results also include power on and off analyses, which indicate reduced thrust-induced drag for the SUSAN Electrofan's DEP and BLI aft fuselage turbofan propulsors when compared to those of the Boeing 737-8-like reference aircraft.

Nomenclature

α	=	Angle of attack
γ	=	Specific heat ratio of air
η_a	=	Adiabatic fan efficiency
η_{trans}	=	Transmission efficiency
$\mathcal{C}_{\text{geo}}$	=	Equality geometric constraints
$\mathcal{G}_{\text{geo}}$	=	Inequality geometric constraints
$\mathcal{K}$	=	Range parameter
$\mathcal{P}$	=	Shaft power
a	=	Speed of sound
b	=	Wing span
D	=	Drag
D_{t-i}	=	Thrust-induced drag
C_D	=	Drag coefficient
C_L	=	Lift coefficient
C_P	=	Pressure coefficient

*Senior Research Scientist/Engineer, Computational Aerosciences Branch, Building N258, AIAA Member, timothy.chau@nasa.gov
†Research Scientist/Engineer, Computational Aerosciences Branch, Building N258, AIAA Member, brandon.lowe@nasa.gov
‡Research Scientist/Engineer, Computational Aerosciences Branch, Building N258, AIAA Member, leonardo.machado@nasa.gov
§Research Scientist/Engineer, Computational Aerosciences Branch, Building N258, AIAA Member, joshua.l.anibal@nasa.gov
¶Branch Chief, Computational Aerosciences Branch, Building N258, AIAA Member, jared.c.duensing@nasa.gov

c_p	=	Specific heat capacity of air
F_x	=	Streamwise force
F_z	=	Vertical force
h	=	Specific enthalpy
L	=	Lift
M	=	Mach number
M_y	=	Pitching moment
$\dot{m}$	=	Mass flow rate
R	=	Gas constant of air
T	=	Thrust
T_t	=	Total temperature
t/c	=	Thickness-to-chord ratio
W	=	Weight
$\mathbf{x}$	=	Design variable vector
x, y, z	=	Cartesian coordinates
y^+	=	Nondimensional off-wall distance

Acronyms

BLI	=	Boundary Layer Ingestion
CFD	=	Computational Fluid Dynamics
DEP	=	Distributed Electric Propulsion
EAP	=	Electrified Aircraft Propulsion
FFD	=	Free-Form Deformation
FPR	=	Fan Pressure Ratio
LAVA	=	Launch, Ascent, and Vehicle Aerodynamics
LE	=	Leading Edge
MFW	=	Maximum Fuel Weight
MTOW	=	Maximum Takeoff Weight
MZFW	=	Maximum Zero Fuel Weight
NPSS	=	Numerical Propulsion System Simulation
OEW	=	Operating Empty Weight
OML	=	Outer Mold Line
PAI	=	Propulsion-Airframe Integration
PSC	=	Power Savings Coefficient
RANS	=	Reynolds-Averaged Navier-Stokes
SA	=	Spalart-Allmaras
SOC	=	Start of Cruise
SUSAN	=	Subsonic Single Aft Engine
TE	=	Trailing Edge
TOC	=	Top of Climb
TSFC	=	Thrust Specific Fuel Consumption
WATE	=	Weight Analysis of Turbine Engines

I. Introduction

The Subsonic Single Aft Engine (SUSAN) Electrofan is a new hybrid electric 180 passenger transport aircraft being developed at NASA, which aims to achieve significant reductions in aviation energy usage and emissions by 2040 [1]. Included is a series hybrid-electric powertrain where an aft fuselage turbofan produces 35% of the total aircraft thrust while also generating electrical power to support wing-mounted electric propulsors that efficiently produce the remaining 65% thrust. This powertrain includes a rechargeable battery to manage power extraction and usage during transient states, while also supporting a parallel hybrid system integrated with the turbofan for augmenting its performance. These electrified aircraft propulsion (EAP) systems enable several advanced propulsion and propulsion-airframe integration

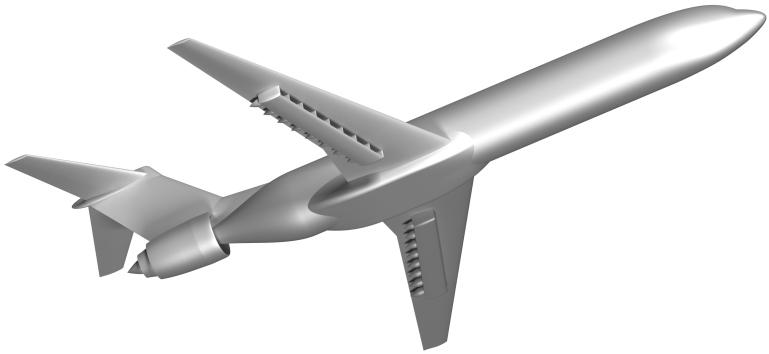


Fig. 1 The SUSAN Electrofan concept, which features wing-mounted DEP systems and a BLI aft fuselage turbofan.

(PAI) technologies, which contribute to the SUSAN Electrofan's energy efficiency. These include distributed electric propulsion (DEP) and boundary layer ingestion (BLI). The current SUSAN Electrofan concept is shown in Figure 1.

The main benefit of DEP is an increase in the effective bypass ratio of a given propulsion system by distributing the thrust produced by a few propulsors across many smaller units with lower fan pressure ratios (FPRs), which together increase the total capture area. This reduces the shaft power required by the propulsion system to produce a given level of thrust. Since the weight of such propulsors scales approximately with the square of the diameter [2, 3], the total weight of such a system is also reduced relative to a comparable non-DEP system. Weight penalties and other system integration challenges from having larger conventional bypass ratio engines, which include increases to landing gear height, are also avoided by DEP. Another benefit of DEP is that it expands the propulsion system design space by enabling beneficial PAI effects. Through a strategic placement of these smaller propulsion units, one can achieve lift enhancement and BLI [4–6], which can lead to system level benefits and further reductions in required shaft power.

The SUSAN Electrofan's turbofan is positioned on the aft fuselage to configure it for BLI, which has been shown to also have the potential for energy savings [7, 8]. Through the ingestion of the low-momentum boundary-layer flow developed over the fuselage, the turbofan can in principle produce a given level of thrust under reduced power requirements. However, several challenges still remain to be addressed. Most prominent among these is inlet distortion, which can impact fan performance and its life cycle. The integration of the turbofan with the fuselage and tail systems of the SUSAN Electrofan must also be considered.

Nonetheless, one of the key questions surrounding the SUSAN Electrofan's DEP and aft fuselage turbofan systems is, what are their benefits when accounting for aerodynamic and aeropropulsive trades in their designs? For instance, although DEP can increase the effective bypass ratio of the complete propulsion system, the amount of wetted area and hence viscous drag increases proportionately with the number of propulsors across which the thrust is being distributed. Although a mail-slot nacelle concept, especially when assuming a BLI configuration as shown in Figure 1, can help to reduce these losses, the first-order aeropropulsive trades must still be sufficiently favorable for a worthwhile net benefit to be achieved. Mail-slot nacelles also give rise to their own challenges, chief amongst these being adverse PAI effects, which may be mitigated through careful design, requiring novel topologies and features [9–11]. Aeropropulsive trade assessments must also be performed for the aft fuselage turbofan, where the benefits of reduced shaft power should be shown to correlate with a reduction in the flow momentum at the inlet. These first challenges can be addressed through the application of computational tools for high-fidelity aeropropulsive design and analysis.

In this paper, aeropropulsive shape optimization based on the Reynolds-averaged Navier-Stokes (RANS) equations is used to develop representative free-flying low-FPR ducted fans to represent the individual propulsors of the SUSAN Electrofan's DEP systems. High-fidelity aerodynamic shape optimization is also used to develop a representative airframe for the SUSAN Electrofan, which includes the fuselage, wing, horizontal and vertical tails, and the BLI aft fuselage turbofan from Machado et al. [12]. Through a decoupled iterative approach, analysis of the representative airframe and propulsion systems enables investigations into the potential benefits of DEP and the BLI aft fuselage turbofan through full-configuration simulations. Although this omits the PAI effects of DEP, which can prove to be adverse [9, 13], this enables an assessment of the technology's performance potential.

Similarly, high-fidelity aeropropulsive and aerodynamic shape optimization is also used to develop a non-DEP

variant of the SUSAN Electrofan, as well as a reference aircraft based on the Boeing 737-8 [14]. Through the same iterative method, forces and moments are balanced to simulate steady, level flight. Assessments of aerodynamic and aeropropulsive performance are then performed, comparing the SUSAN Electrofan concept to the non-DEP variant and the Boeing 737-8-like reference aircraft. This provides a means for assessing the aeropropulsive benefits of the SUSAN Electrofan's DEP and BLI aft fuselage turbofan technologies while accounting for differences in airframe aerodynamic performance.

The present paper is organized as follows. Section II provides an overview of the technology assessment method, Section III presents the aircraft concepts, characteristics, and operating conditions, and Section IV describes the high-fidelity aerodynamic and aeropropulsive shape optimization frameworks. Sections V and VI then present the development of the representative airframes and wing propulsors through the application of computational fluid dynamics (CFD)-based optimization. The full-configuration aircraft performance assessments are then presented in Section VII, with conclusions and future work outlined in Section VIII.

II. Overview of the Technology Assessment Methodology

In order to estimate the benefits of the SUSAN Electrofan's DEP and BLI aft fuselage turbofan technologies, representative aircraft models are developed in 3D and compared with one another using aeropropulsive CFD simulations based on the RANS equations. This includes aircraft models of the SUSAN Electrofan with and without its wing-mounted DEP systems and an aircraft model based on the Boeing 737-8. These aircraft models consist of airframe and propulsion system models, with the wing-mounted propulsion systems simulated separately as simplified free-flying ducted fans based on the method of Gray and Martins [15].

Although this omits both positive and negative PAI effects relevant to the viability and feasibility of DEP technology for transonic transport aircraft, modeling the wing-mounted propulsors in free-air substantially reduces the complexity of developing representative wing and propulsor designs. Moreover, it allows for a focus on one of the main benefits of DEP technology: reductions in the shaft power required to produce a given level of thrust via high effective bypass ratios, which must trade against the cost of higher viscous drag. This represents a step forward from more conceptual-level models of DEP systems [16], which capture the benefits of ultra-high effective bypass ratios to first order but do not properly account for the drag penalties associated with having many small individual propulsors. Nonetheless, investigations into the integrated design of the SUSAN Electrofan's DEP systems are a part of ongoing work involving high-fidelity aeropropulsive design and analysis, see for example Machado et al. [9, 12, 13] and Anibal and Duensing [11]. Conversely, PAI effects are essential to the benefit of the BLI aft fuselage turbofan: reductions in the shaft power required to produce a given level of thrust via the ingestion of low-momentum boundary-layer flow [17]. Therefore, the configurations that include this technology have them integrated with their airframes.

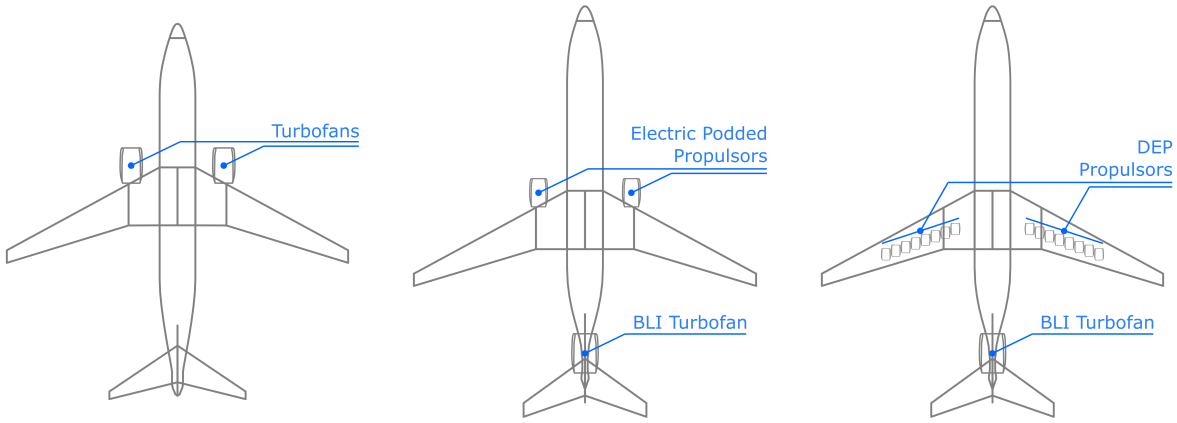
Figure 2 illustrates the aircraft concepts used to develop the representative airframe and propulsion system models. Figures 2a and 2c show the Boeing 737-8 and SUSAN Electrofan concepts, respectively, while Figure 2b shows the additional reference aircraft used to estimate the relative benefits of the SUSAN Electrofan's DEP technology more directly. These aircraft concepts are described as follows.

B737-8: This aircraft concept represents the Boeing 737-8 and serves as a year 2020 technology level reference aircraft for performance comparisons against the SUSAN Electrofan. The airframe consists of a wing, fuselage, and fairing, and a conventional tail system. The propulsion system includes two underwing turbofans.

SUSAN-Pod: This aircraft concept is a non-DEP reference variant of the SUSAN Electrofan. The airframe consists of the SUSAN Electrofan's wing, fuselage, fairing, and integrated T-tail system. The propulsion system includes two electric underwing propulsors, which are sized for a similar level of thrust as the DEP systems of the SUSAN Electrofan, a BLI aft fuselage turbofan, and a hybrid-electric powertrain.

SUSAN-DEP: This aircraft concept represents the SUSAN Electrofan. The airframe consists of a wing, fuselage, and fairing, and an integrated T-tail system. The propulsion system includes wing-mounted DEP systems with a total of 16 ducted fans, a BLI aft fuselage turbofan, and a hybrid-electric powertrain.

Note that although the SUSAN-Pod concept differentiates itself sufficiently from the SUSAN Electrofan to justify the development of its own conceptual model, this work assumes that relevant aircraft level characteristics, such as weight, cruise lift coefficient, and operating conditions, are approximately equal to those of the nominal configuration to first order. Therefore, both variants of the SUSAN Electrofan are developed based on the top-level aircraft requirements of the nominal configuration, presented in Section III. Similarly, since the current version of the SUSAN Electrofan is



(a) B737-8 **(b) SUSAN-Pod** **(c) SUSAN-DEP**

Fig. 2 Aircraft concepts used to develop representative aircraft configurations for assessing the SUSAN Electrofan's DEP and BLI aft fuselage turbofan technologies.

assumed to have its propulsion systems sized to the same thrust requirements as those of the Boeing 737-8 [18], the propulsion systems of the SUSAN-Pod configuration are also developed to meet these requirements.

With the representative full-configuration aircraft models, the SUSAN Electrofan's DEP and BLI aft fuselage turbofan technologies are assessed via the power balance method [15, 19], where each airframe and propulsion system combination is iteratively trimmed in streamwise power via thrust inputs to the propulsion system models. Lift and pitching moment are also trimmed for each aircraft configuration. Relative performance is then given by the power savings coefficient [20, 21],

$$\text{PSC} = \frac{\mathcal{P} - \mathcal{P}_{\text{ref}}}{\mathcal{P}_{\text{ref}}} \tag{1}$$

where $\mathcal{P}$ is the shaft power required by the propulsion systems of a given aircraft configuration to be trimmed, and $\mathcal{P}_{\text{ref}}$ is the equivalent shaft power required by a given reference aircraft. This method captures the differences in drag associated with each of the aircraft configurations, as well as PAI effects included in the CFD simulations.

In this work, the total shaft power is given by the sum of the shaft power required by N propulsors [15]:

$$\mathcal{P} = \sum_{i=1}^{N} \mathcal{P}_i = \sum_{i=1}^{N} \frac{\dot{m}_i \Delta h_i}{(\eta_{\text{trans}})_i} \tag{2}$$

where, for propulsor i, $\dot{m}_i$ is the mass flow rate, Δh_i is the change in specific enthalpy across a given fan, and $(\eta_{\text{trans}})_i$ is the end-to-end electrical transmission efficiency of the hybrid-electric powertrain for electric propulsors (see Section III) and unity for turbofans. The change in specific enthalpy is calculated as

$$\Delta h = c_p \left(T_{t_3} - T_{t_0}\right) = \frac{1}{\eta_a} \left(\frac{\gamma R}{\gamma - 1}\right) T_{t_0} \left(\text{FPR}^{\frac{\gamma-1}{\gamma}} - 1\right) \tag{3}$$

where c_p, γ, and R are the specific heat capacity, specific heat ratio, and gas constant of air, respectively, and T_{t_0} and T_{t_3} are the total temperature at the fan inlet and exit, respectively. The adiabatic fan efficiency, η_a, is calculated based on the method of Gray [22],

$$\eta_a = 1.066 - 0.0866\ \text{FPR} \tag{4}$$

which is a linear regression based on advanced subsonic transport aircraft.

In this method, the shaft power required by a given propulsor reduces with specific enthalpy change. This can be achieved through lower FPRs, which improves adiabatic fan efficiency. For the same level of thrust, a reduction in FPR can be achieved by increasing mass flow rate or through the ingestion of low-momentum boundary-layer flow. Naturally, FPR can also be reduced by reducing thrust levels, which corresponds to reductions in cruise drag.

The aircraft configurations are also assessed based on the range parameter, a measure of cruise efficiency [23, 24] that accounts for differences in aerodynamic and propulsion system performance. The range parameter is given by,

$$\mathcal{K} = \frac{aM}{\text{TSFC}}\left(\frac{L}{D}\right) \tag{5}$$

where a and M are the speed of sound and Mach number, respectively, TSFC is the thrust specific fuel consumption, and L/D is the lift-to-drag ratio. In the present paper, the aerodynamic range efficiency $M(L/D)$ is computed through CFD, while TSFC is determined from conceptual models of the Boeing 737-8's and SUSAN Electrofan's propulsion systems, as described in Section III.

III. Aircraft Concepts, Characteristics, and Operating Conditions

The aircraft concepts of the B737-8 and the SUSAN Electrofan form the basis of the high-fidelity aerodynamic and aeropropulsive shape optimizations presented in Sections V and VI, respectively, and the high-fidelity aerodynamic and aeropropulsive assessments that follow. These concepts are obtained through the application of a conceptual multidisciplinary design analysis and optimization framework called Faber [25], and represent updates to the conceptual models presented in Chau and Duensing [18]. Specifically, altitude design variables are introduced, as well as updated disciplinary models and key performance parameters (KPPs) related to the SUSAN Electrofan's EAP systems. These include an updated NPSS and WATE++ propulsion system model, which introduces the most recent nominal electrical component efficiencies presented in Chau and Duensing [18], as well as updated thermal management system weights and drag penalties from recent work by Stalcup et al. [26].

Table 1 provides an overview of the aircraft characteristics for the B737-8 and the SUSAN Electrofan. As described in Chau and Duensing [18], for the SUSAN Electrofan, the main goal of the aircraft sizing problem is to develop an aircraft concept based on the overall sizing of the Boeing 737-8, but with significantly reduced energy usage and emissions through the advantages of DEP and BLI technology, and a hybrid electric propulsion system architecture. Toward this end, the SUSAN Electrofan is designed for Mach 0.785 with a maximum passenger payload of 180 passengers. Its overall sizing is also driven by constraints on the design wing loading and thrust-to-weight ratio, as well as top of climb (TOC) thrust requirements, all based on the Boeing 737-8. However, to accommodate the increase in weight that comes from the EAP systems, the SUSAN Electrofan is developed for reduced design and economy ranges of 2,500 nmi and 750 nmi, respectively. This reduces aircraft fuel weight, which, when combined with fuel weight reductions achieved through improvements to aircraft efficiency, helps mitigate more significant increases in overall aircraft weight. These range capabilities position the SUSAN Electrofan for the regional jet market [27].

Although the aircraft sizing problem of the SUSAN Electrofan is defined based on the Boeing 737-8, the conceptual design optimizations result in higher maximum takeoff weight (MTOW), maximum zero fuel weight (MZFW), and operating empty weight (OEW). MTOW, for example, is 4.8% higher for the SUSAN Electrofan, which can be attributed primarily to its 17% higher OEW. This leads to higher aircraft weights at cruise for a similar level of climb fuel weight, and hence higher cruise lift requirements. This motivates the need to optimize the initial cruise altitude of the SUSAN Electrofan for a given mission, since trades across the various disciplines need to be adjusted accordingly to maintain optimum block fuel burn. Thus, the conceptual design problems in Chau and Duensing [18] are repeated but with altitude design variables included. The conceptual modeling of the B737-8 is also repeated with altitude design variables for fair comparisons.

In order to account for thermal drag as a function of cruise altitude and time, which is caused by heat rejection from the electrical component losses, the previous SUSAN Electrofan aircraft concept was used to generate reference mission profiles at several initial cruise altitudes for both the design and economy range missions. This was done assuming similar climb and descent schedules. These reference missions were then used to size and analyze the thermal management system, as presented in Stalcup et al. [26]. Based on the thermal drag penalty profiles from this study, thermal drag is interpolated for a given altitude design variable.

Initial aircraft optimizations resulted in relatively high cruise lift coefficients for the B737-8 and the SUSAN Electrofan, presumably from the optimistic conceptual wave drag models, as well as the unavailability of a reliable model for buffet onset prediction at the conceptual level. Therefore, a 10% markdown on the start of cruise lift coefficient was introduced as a constraint, and the concepts were re-optimized. This results in a design cruise lift coefficient of 0.556 and 0.589 for the B737-8 and SUSAN Electrofan, respectively, based on their economy range missions. These correspond to initial cruise altitudes of 36,720 ft and 37,000 ft, respectively, which are used to define the high-fidelity aerodynamic and aeropropulsive design and analysis problems of each aircraft configuration.

Table 1 Aircraft characteristics for the conceptual models of the B737-8 and the SUSAN Electrofan.

Parameter	B737-8	SUSAN	Δ
Mean aerodynamic chord (ref.), ft	13.79	14.52	+5.3%
Wing area (gross, ref.), ft^2	1,396	1,485	+6.4%
Wing span, ft	117.83	117.83	+0.0%
Wing aspect ratio	9.95	9.35	−6.0%
Wing sweep (LE), deg	28.5	28.5	+0.0%
Horizontal tail area, ft^2	360	397	+10.3%
Vertical tail area, ft^2	278	270	+2.9%
Wing loading, lb/ft^2	130.3	128.4	−1.5%
Thrust-to-weight ratio	0.297	0.298	+0.3%
MTOW, lb	181,870	190,610	+4.8%
MZFW, lb	145,450	165,850	+14.0%
OEW, lb	99,450	119,850	+17.0%
MFW, lb	46,920	34,140	−27.2%
Design payload, lb	39,600	39,600	+0.0%
Design range, nmi	3,100	2,500	−19.4%
Economy range, nmi	1,000	750	−25.0%
Mach number (SOC)	0.785	0.785	+0.0%
Altitude (SOC), ft	36,720	37,000	+0.8%
Reynolds number (SOC), $\times 10^6$	24.14	25.07	+3.9%
Lift coefficient (SOC)	0.556	0.589	+5.9%
TSFC (SOC), lb/lbf/hr	0.5593	0.4550	−18.6%

It should be noted that the EAP system sizing process was repeated from Chau and Duensing [18], where the EAP system weight KPPs, which have the most impact on aircraft sizing, are determined based on top-level aircraft requirements. The SUSAN Electrofan concept presented in this section corresponds to an EAP system weight technology factor of 6.7 on a scale from 1 to 10 where 1, 5, and 10 correspond to conservative, nominal, and optimistic technology level projections, respectively. For the EAP system electrical component efficiencies, nominal technology factors are assumed [18]. This provides an end-to-end electrical transmission efficiency of 90%, which is used in Section VII to calculate the shaft power required by the electric propulsors.

It should also be noted that the SUSAN Electrofan has the benefit of an 18.6% lower TSFC relative to the B737-8. As described in Chau and Duensing [18], this comes from several advantages of the SUSAN Electrofan's hybrid electric propulsion system. Included are a geared turbofan design with advanced technology levels assumed for its turbomachinery components, a larger turbofan core flow that results in an overall pressure ratio more than double that of the CFM LEAP-1B, and the Turbine Electrified Energy Management concept [28, 29], which improves the operability of the turbofan. This also accounts for the ultra-high effective bypass ratio enabled by the SUSAN Electrofan's DEP systems and the benefits of aft fuselage turbofan BLI, modeled to first order. For the SUSAN-Pod configuration, TSFC is approximated by scaling the SUSAN Electrofan's TSFC by the relative shaft power of the SUSAN-Pod and SUSAN-DEP configurations in order to remove the benefits of DEP.

IV. Computational Design and Analysis Frameworks

This section provides a brief overview of the computational tools for aerodynamic and aeropropulsive design and analysis. This includes an aerodynamic shape optimization framework based on the RANS equations for developing representative airframe models, and a RANS-based aeropropulsive shape optimization framework for developing

representative wing propulsors. This also includes a RANS-based flow solver for aeropropulsive analysis.

A. High-Fidelity Aerodynamic Shape Optimization Framework

Aerodynamic shape optimization is provided by the Launch, Ascent, and Vehicle Aerodynamics (LAVA) framework [30], which has been recently extended to include gradient-based optimization capabilities [31]. Although this framework allows for flow solutions on unstructured polyhedral and structured Cartesian grids, the present paper uses the curvilinear overset grid paradigm, which is well-suited to the external aerodynamics problems considered in this work.

The LAVA curvilinear flow solver is used to solve the RANS equations, with closure provided by the one-equation Spalart-Allmaras (SA) turbulence model [32]. More specifically, SA-RC-QCR2000 is used, which includes rotation curvature (RC) corrections [33] and quadratic constitutive relations (QCR) [34], and boundary layers are assumed to be fully turbulent. Convective fluxes of the mean flow equations are evaluated with a modified Roe scheme via third-order upwind flux reconstruction and the Koren flux limiter [35, 36]. Convective terms of the turbulence model are discretized using a first-order upwind scheme. Viscous fluxes in the momentum, total energy, and turbulence model equations are discretized with a second-order mid-point and node scheme. Steady-state solutions are computed using an efficient parallel implicit approximate Newton-Krylov algorithm. At each Newton iteration, the mean flow and turbulence model equations are decoupled and solved independently using the preconditioned generalized minimal residual (GMRES) method [37]. The preconditioner is obtained from an incomplete lower-upper factorization of a first-order approximation of the residual Jacobian.

The influence of propulsors on the steady-state flow can be modeled within the LAVA curvilinear flow solver using actuator zone and actuator blade methods [38]. In the present paper, the actuator zone method is used with source terms distributed uniformly based on a specified thrust. These source terms are applied to the governing flow equations over a subset of computational nodes within the grid and add momentum and energy. Although a user-specified torque can also be provided to augment the momentum and energy source terms, reference blade models from which torque inputs can be derived are not included in the current work.

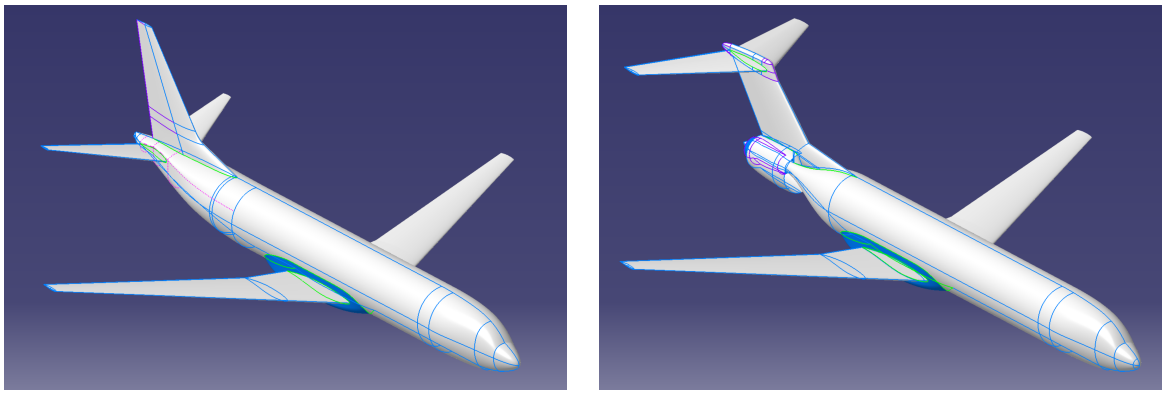
Gradient-based optimization is performed through SNOPT [39]. For objective function and constraint gradients that depend on the flow solution, the LAVA framework uses the discrete-adjoint method, with partial derivatives of the flow functionals and residual computed through a combination of automatic differentiation and analytic hand-differentiation. The discrete adjoint equation is solved using the generalized conjugate residual with inner-orthogonalization and deflated restarting (GCRO-DR) method [40] with iterative refinement.

Geometry control and parameterization is provided by the free-form deformation (FFD) method [41] applied through the open source package pyGeo [42]. Mesh deformation is performed through an implementation of the approximate inverse distance weighted approach of Secco et al. [43] within the LAVA framework, with deformations of surface meshes near component intersections controlled by the method of Yildirim et al. [21].

B. High-Fidelity Aeropropulsive Shape Optimization Framework

Although the LAVA framework can perform CFD-based aeropropulsive analysis with its actuator zone capabilities, the infrastructure for high-fidelity aeropropulsive optimization has not yet been implemented. Thus, the present work uses the Multidisciplinary Design Optimization of Aircraft Configurations with High Fidelity (MACH)-Aero framework, an open-source optimization framework that can meet this need. MACH-Aero uses IDWarp [43] for mesh deformation and ADflow [44] for solving the RANS equations coupled with the SA turbulence model. Within ADflow is a structured multiblock second-order finite-difference flow solver used in this work, which is based on an efficient parallel implicit approximate Newton-Krylov alogrithm similar to the LAVA curvilinear flow solver. ADflow also uses the discrete-adjoint method [45, 46] with AD [47] to support gradient-based optimization using SNOPT [39]. ADflow also includes an actuator zone method [15] comparable to that of the LAVA curvilinear flow solver. For geometry control, although MACH-Aero includes FFD capabilities, the present work uses NASA's OpenVSP software [48], which was found to offer a more natural geometry parameterization for nacelle and hub geometries through Bézier curves and B-splines.

Although ADflow has much in common with the LAVA curvilinear flow solver, post-optimization aeropropulsive analysis will be performed with the latter to maintain consistency with the aerodynamics analysis performed on the optimized airframes. This consistency will be important when estimating full-configuration aircraft performance.



(a) B737-8 (b) SUSAN

Fig. 3 Baseline airframe models used to perform aerodynamic shape optimization.

V. Representative Airframe Designs

This section presents the problem formulations and results of the aerodynamic shape optimizations used to develop representative airframe models for the full-configuration aircraft performance evaluations. The aircraft concepts presented in Section III are first used to develop detailed baseline wing–body–tail models in 3D. Aerodynamic shape optimization is then applied to the wing and horizontal tail designs of each configuration with the objective of minimizing cruise drag at constant lift and zero pitching moment. These airframe models will be used together with the representative propulsor designs to estimate the shaft power required to trim each aircraft via the power balance approach.

A. Baseline Airframe Models

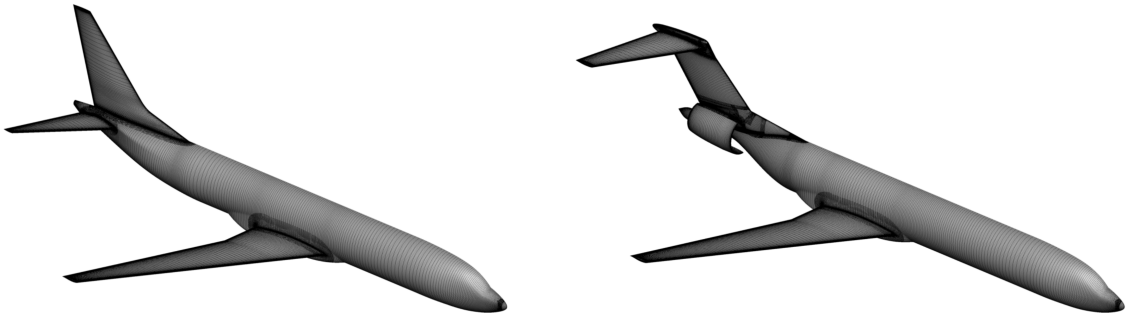
In order to develop representative airframe models through aerodynamic shape optimization, baseline geometries must first be developed in 3D. Toward this end, baseline wing–body–tail models are developed based on the conceptual models presented in Section III. These airframe models are shown in Figure 3, where the overall dimensions of the aircraft components are determined from the conceptual models. Details such as the outer mold line (OML) of the fuselage nose and tail sections are modeled based on the aircraft drawings included in the Boeing 737-8's airport planning manual [14].

Since aerodynamic shape optimization will be used to design the OML of the wing systems, the baseline wing designs of both airframes are untwisted and defined by RAE 2822 airfoils, which provide a good starting point for gradient-based optimization at transonic conditions. The horizontal tails are also untwisted and defined by NASA SC(2)-0012 airfoils. For the B737-8, NACA 64-012A airfoils are used for the vertical tail based on the work of Atinault and Hue [49], while for the SUSAN Electrofan, airfoils similar to the NACA 0012 are selected for their forward maximum thickness locations at approximately 30% chord. A bullet fairing based on the McDonnell Douglas MD-80 [50] is also included at the tip of the SUSAN Electrofan's vertical tail to reduce interference drag with the horizontal tail.

For the SUSAN Electrofan, the previous aft fuselage turbofan design [12] is re-integrated with the fuselage and T-tail system through the integrated structural design concept presented by Jansen et al. [1]. The main component is a dorsal fin that provides the majority of the structural support. The dorsal fin also transitions smoothly to a splitter at the inlet, intended to be incorporated with an array of inlet guide vanes to reduce flow distortion. In the current work, however, these inlet guide vanes are omitted to reduce the computational cost of performing high-fidelity aerodynamic shape optimization.

B. Airframe Computational Grids

The computational domain around each airframe geometry is discretized with structured overset meshes. The structured overset mesh paradigm is a grid generation method that can be advantageous when considering complex geometries due in part to its modular approach, which provides a good balance between grid generation time, grid quality, and space-filling efficiency. For optimization, these grids are created based on the coarse mesh resolution of the Seventh Drag Prediction Workshop (DPW-VII) [51] in order to keep the computational cost associated with performing



(a) B737-8 **(b) SUSAN**

Fig. 4 Optimization level surface meshes for the baseline geometries.

Table 2 Airframe grid information for performing aerodynamic shape optimization (L0) and grid refinement studies (L0, L1, and L2).

Grid	Refinement Factor	Number of Nodes	Average y^+
B737-8			
L0	1.00	9.88×10^6	0.61
L1	1.40	26.81×10^6	0.45
L2	2.00	78.09×10^6	0.29
SUSAN			
L0	1.00	13.90×10^6	0.66
L1	1.40	37.26×10^6	0.48
L2	2.00	108.94×10^6	0.31

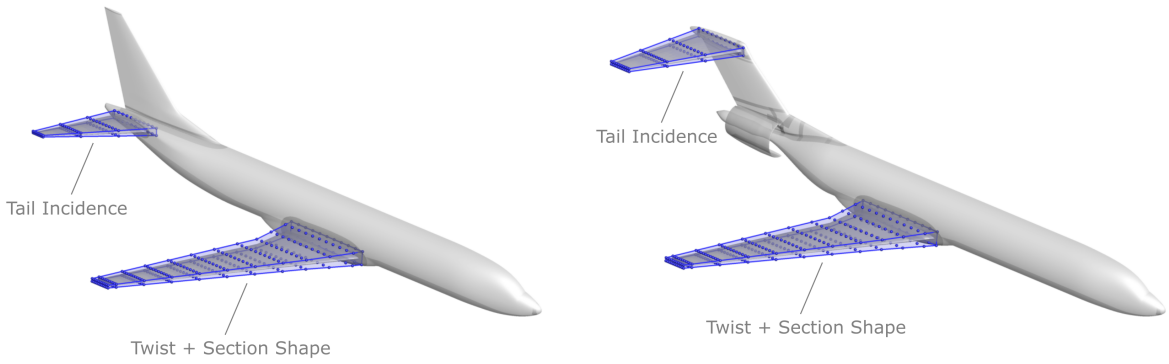
[1] y^+ values are based on baseline geometry analysis at cruise conditions.

hundreds of flow and adjoint solves at reasonable levels. However, in order to improve the accuracy of performance evaluations, aerodynamic functionals are estimated through Richardson extrapolation using two additional grid levels, L1 and L2, with refinement factors of 1.4 and 2.0, respectively, along each coordinate direction. These grid convergence studies will be presented in Section VII as a part of the power balance results. The computational domains also only include half-span models to further reduce computational cost.

For the SUSAN Electrofan, the aft fuselage turbofan includes actuator zone volume grids for modeling the thrust produced by the fan. However, since the turbofan is not expected to largely affect the design of the wing and tail systems, and the thrust contribution is assumed to have a negligible impact on lift and pitching moment at cruise angles of attack, only flow-through conditions are considered during optimization. Similarly, the turbofan core is removed to further simplify the optimization problem. Figure 4 shows the surface meshes for each airframe on the optimization grid level, L0. Table 2 provides a summary of the grid characteristics.

C. Airframe Optimization Problems

The main goal of the aerodynamic shape optimizations is to develop airframe models with representative aerodynamic design characteristics and performance at cruise. Toward this end, aerodynamic shape optimization is primarily applied to the detailed design of the wing of each aircraft configuration, with the objective of minimizing drag while subject to



(a) B737-8 **(b) SUSAN**

Fig. 5 Airframe design geometry control systems with FFD volume entities in blue.

constant lift and zero pitching moment constraints. More formally, the optimization problems are defined as follows:

$$\begin{aligned} \text{minimize} \quad & C_D \\ \text{w.r.t.} \quad & \mathbf{x} \\ \text{s.t.} \quad & L = W, \quad M_y = 0 \\ & C_{\text{geo}} = 0, \quad \mathcal{G}_{\text{geo}} \leq 0 \end{aligned}$$

where C_D is the cruise drag coefficient, $\mathbf{x} = [\alpha, \mathbf{x}_{\text{geo}}^{\text{T}}]^{\text{T}}$ is the design variable vector, which includes angle of attack, α, and the vector of geometric design variables, $\mathbf{x}_{\text{geo}}$, and C_{geo} and $\mathcal{G}_{\text{geo}}$ are the geometric equality and inequality constraints, respectively.

Figure 5 shows the FFD volume geometry control systems, which define the geometric design variables. In this method, FFD volumes are used to smoothly deform embedded objects, namely, the wing and horizontal tail of each aircraft configuration. These FFD volumes are B-spline volumes whose control points can be used to drive the deformations. Specifically, the xyz-coordinates of the B-spline control points are used to define twist and section shape design variables, where twist is a rotation of a given FFD-volume cross-section about the local origin, and section shape is a vertical scaling of an FFD-volume control point's initial coordinates along the local z-axis. In this work, the local coordinate systems are defined at the $1/4$-chord of each wing and at approximately the $1/2$-chord of each horizontal tail.

Given that each aircraft configuration has the same wing and horizontal tail topologies, their FFD volumes are defined by the same number of FFD-volume cross-sections and control-point pairs. With regard to degrees of freedom, the wing FFD volumes include one twist design variable per FFD-volume cross-section and one section shape design variable per FFD-volume control point. However, the horizontal tail FFD volumes only include twist design variables, which are linked across the FFD-volume cross-sections to yield a single tail incidence degree of freedom. This is done to maintain the symmetric section shape designs of the horizontal tails while allowing them to aid in satisfying the pitching moment constraint. Other design variables such as chord, sweep, span, and dihedral are not included in order to minimize the impact of the aerodynamic designs on non-aerodynamics disciplines and off-design performance. Table 3 provides a summary of the design variables and their bounds.

Geometric constraints include minimum wing volume, minimum t/c scaling, and minimum $(t/c)_{\text{max}}$, where t is the airfoil thickness and c is the chord. These are used to maintain sufficient wing volume for the fuel tanks, which are sized based on the maximum fuel weight (MFW) of each aircraft, and to ensure a minimum structural depth, both determined by the conceptual modeling process. The local z-displacements of FFD-volume control points at the leading edge (LE) and trailing edge (TE) of the wing are also constrained to prevent shear twist and translation of the wing system. A summary of the constraints is provided in Table 4.

D. Airframe Optimization Results

The airframe design optimizations completed in 203 and 218 function evaluations for the B737-8 and SUSAN Electrofan configurations, respectively. The objective function converged to a tenth of a drag count and constraint

Table 3 Aerodynamic shape optimization design variables.

Design Variable	Quantity	Lower Bound	Upper Bound
Angle of attack	1	−3.0 deg	+3.0 deg
Wing			
Twist	12	−10.0 deg	+10.0 deg
Section shape	264	0.5	2.0
Horizontal tail			
Twist	4	−10.0 deg	+10.0 deg
Total	281	— —	— —

Table 4 Aerodynamic shape optimization constraints.

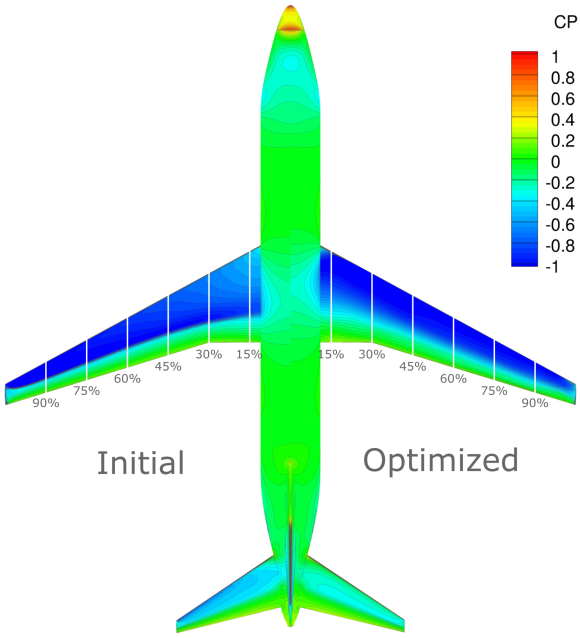
Constraint	Quantity	Description
Lift	1	Constrains the aircraft lift to equal the weight at cruise (nonlinear)
Pitching moment	1	Constrains the aircraft pitching moment to equal zero at cruise (nonlinear)
Minimum wing volume	1	Constrains the minimum wing OML volume based on fuel storage requirements (nonlinear)
Minimum $(t/c)_{\max}$	12	Minimum maximum thickness-to-chord ratio constraints based on structural requirements (nonlinear)
Minimum t/c scaling	132	Constrains the local vertical separation between each pair of FFD-volume control points to be greater than or equal to 80% of its initial value (linear)
Fixed LE/TE	24	Constrains section shape design variables at the LE and TE to be equal and opposite between the lower and upper FFD-volume control points (linear)
Linked horizontal tail twist	3	Links the twist design variables of the horizontal tail (linear)
Total	174	— —

violations are satisfied to a tolerance of 10^{-6} or less. Figures 6 and 7 provide an overview of the initial and optimized designs and flow features for the airframes of the B737-8 and SUSAN Electrofan, respectively. Based on Figures 6a and 7a, it can be seen that the optimizer is successful in mitigating shock formation from the upper wing surfaces of the initial designs. This is consistent with Figures 6c and 7c where the steep adverse pressure gradients on the upper surface of the initial designs are smoothed to achieve gradual pressure recoveries post-optimization. The root airfoils of both optimized designs also feature a lower surface inset, which increases the local pressure forward on the wing to aid in satisfying the pitching moment constraint. Since the moment arm is reduced for the SUSAN Electrofan due to the geometric limitations imposed by tail-strike considerations in its conceptual design [52], its inset is more pronounced than that of the B737-8. Figures 6b and 7b provides a top view of the upper wing surface pressure distributions. Here it can be seen that the isobars are well-aligned with the geometric sweep angles of the wings, indicating good wave drag performance despite the single-point optimization objective.

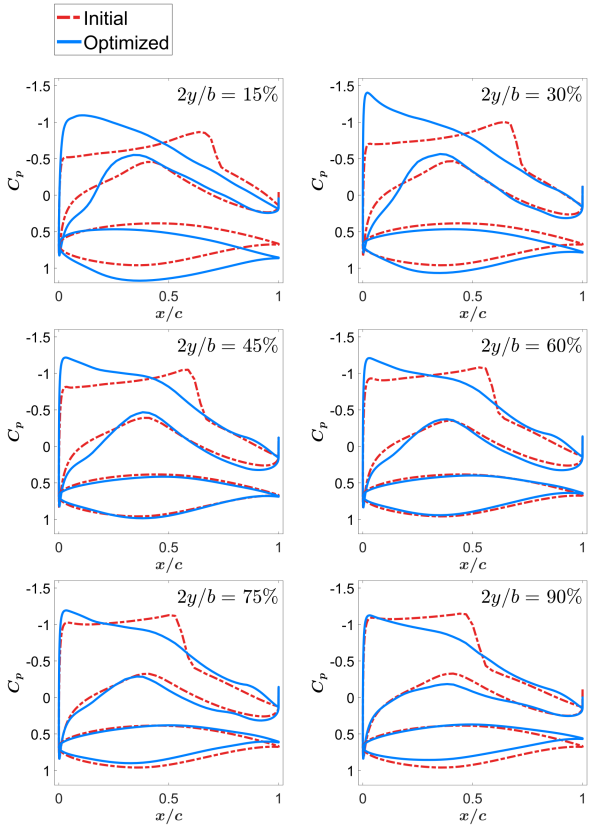
Table 5 provides a summary of the optimized aerodynamic performance for the B737-8 and SUSAN Electrofan airframes. These values are computed on the coarse L0 grid levels, and are only intended to convey aerodynamic design and performance trades. Based on these results, the SUSAN Electrofan experiences 19.3% more drag than the B737-8, which can be attributed to the drag of the aft fuselage turbofan nacelle, as well as drag from the integrated T-tail system. The wing and tail systems are also generally larger than those of the B737-8 due to the SUSAN Electrofan's overall sizing, as indicated by its larger MTOW. The higher weight at cruise due to the weight of the EAP systems also leads to 10.9% more lift, which invariably results in higher induced drag. Although the SUSAN Electrofan requires less tail



(a) Shock surfaces



(b) Surface pressure contours



(c) Airfoil profiles and pressure distributions

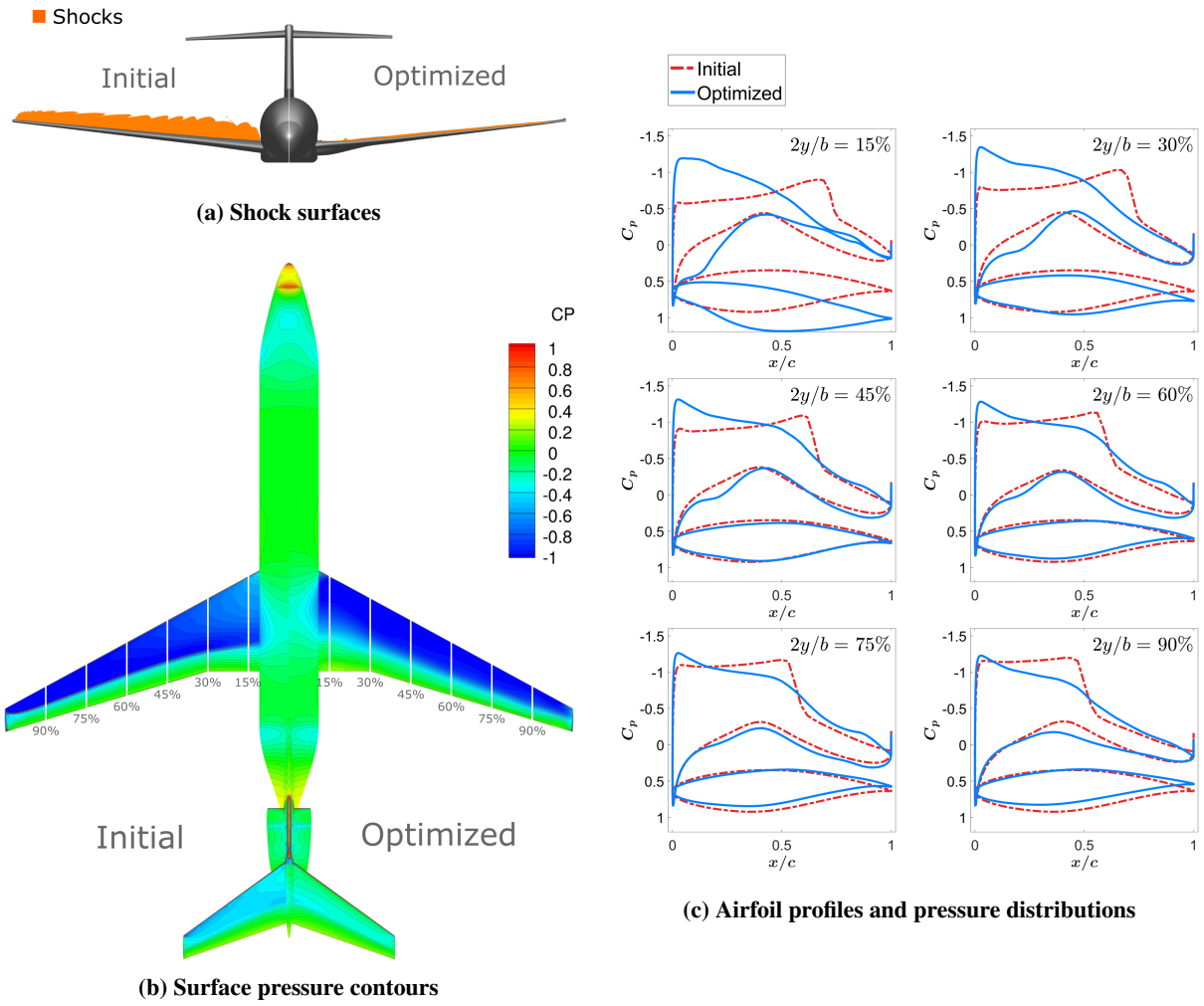
Fig. 6 B737-8: Initial and optimized airframe design and flow features. Flow solutions are computed on the L0 grid level at $M = 0.785$ and $C_L = 0.556$.

deflection to trim the pitching moment on the L0 grid compared to the B737-8, the grid-converged tail incidence angles are estimated to be −2.46 deg and −2.52 deg through Richardson extrapolation for the B737-8 and SUSAN Electrofan, respectively. This further suggests higher trim drag for the SUSAN Electrofan due to its reduced moment arm.

Overall, these results demonstrate that the aerodynamic shape optimizations were successful in developing airframe designs with reasonable design features and good transonic performance, and hence are deemed reasonable representations of the aircraft concepts. These airframes are used in the full-configuration aircraft assessments presented in Section VII.

VI. Representative Wing Propulsor Designs

In this section, high-fidelity aeropropulsive shape optimization is applied to the design of the representative wing-mounted propulsors used to assess full-configuration aircraft performance in Section VII. These propulsor designs are simplified geometries consisting of only a nacelle and hub, and represent (1) the LEAP-1B turbofan for the B737-8, (2) an electric podded propulsor for the non-DEP configuration of the SUSAN Electrofan, and (3) an electric podded propulsor for the DEP configuration of the SUSAN Electrofan. These propulsors are herein referred to as the Turbofan-147, the Pod-147, and the DEP-125, respectively.



(a) Shock surfaces

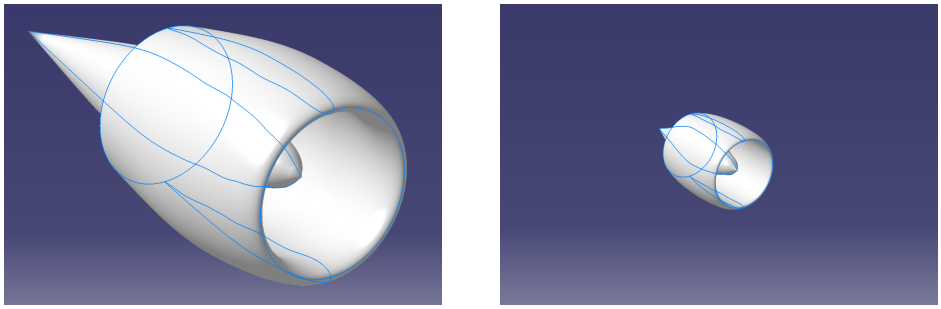
(b) Surface pressure contours

(c) Airfoil profiles and pressure distributions

Fig. 7 SUSAN: Initial and optimized airframe design and flow features. Flow solutions are computed on the L0 grid level at $M = 0.785$ and $C_L = 0.589$.

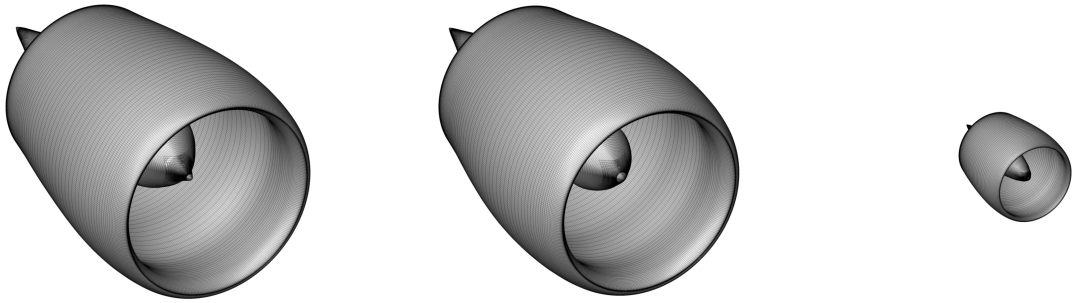
Table 5 Optimized airframe aerodynamic performance computed on the L0 grid level at M = 0.785. Airframes include the fuselage, wing, and horizontal and vertical tails. The SUSAN Electrofan also includes a flow-through aft fuselage turbofan nacelle with no core.

Parameter	B737-8	SUSAN	Δ
Angle of attack, deg	3.00	3.00	—
Tail incidence angle, deg	-2.57	-2.47	—
L/D	19.9	18.5	−7.0%
C_L	0.556	0.589	+5.9%
C_D	0.0279	0.0318	+14.0%
Lift, lb	152,480	169,130	+10.9%
Drag, lb	7,720	9,210	+19.3%



(a) Turbofan-147/Pod-147 (b) DEP-125

Fig. 8 Baseline wing propulsor models used to perform aeropropulsive shape optimization.



(a) Turbofan-147 (b) Pod-147 (c) DEP-125

Fig. 9 L0 grid level surface meshes used to perform grid convergence studies.

A. Baseline Wing Propulsor Models

The Turbofan-147 and Pod-147 propulsors have in common a baseline model developed from the R4 fan [53]. The R4 fan was designed by General Electric and is considered a good representation of modern high-bypass ratio turbofans. The Turbofan-147 and Pod-147 propulsors both have a design FPR of 1.47, with the Turbofan-147 sized to produce 50% of the total thrust share per propulsor, and the Pod-147 sized to produce 32.5% of the total thrust share per propulsor. For the DEP-125 propulsor, the baseline model is developed based on the turbo-electric propulsors of the NASA N3-X hybrid-wing-body as presented in Lee et al. [54]. The total thrust share of the DEP-125 is 4.0625% per propulsor. These baseline propulsor designs are shown in Figure 8 and provide a good starting point for aeropropulsive shape optimization, where appropriate design changes can be introduced to account for differences in the thrust requirements. For more details on the baseline models, see Machado et al. [12].

B. Computational Wing Propulsor Grids

For aeropropulsive shape optimization, relatively coarse grids are used to reduce computational cost. Given the simplicity of the geometries, it is not expected that finer grids are necessary for the design process. However, following optimization, refined grids are used to perform post-optimization grid convergence studies. These grids are developed based on the structured overset mesh paradigm and are used with the LAVA curvilinear flow solver. Figure 9 shows the surface meshes for each of these grids on the L0 grid level. The finer grid levels, L1 and L2, are generated from the L0 grid using refinement factors of 1.4 and 2.0, respectively, along each coordinate direction. Table 6 provides a summary of the grid characteristics for each grid family.

C. Wing Propulsor Optimization Problems

Aeropropulsive shape optimization is used to size and optimize each propulsor design. For all propulsors, the design point is the TOC condition. Since the SUSAN Electrofan is assumed to be sized based on the thrust requirements of

Table 6 Propulsor grid information for performing grid convergence studies.

Grid	Refinement Factor	Number of Nodes	Average y^+
Turbofan-147			
L0	1.00	11.90×10^6	0.54
L1	1.40	31.86×10^6	0.36
L2	2.00	93.12×10^6	0.25
Pod-147			
L0	1.00	11.77×10^6	0.54
L1	1.40	31.91×10^6	0.33
L2	2.00	93.34×10^6	0.23
DEP-125			
L0	1.00	6.03×10^6	0.57
L1	1.40	15.92×10^6	0.41
L2	2.00	46.85×10^6	0.28

the Boeing 737-8, all propulsors are sized for a TOC aircraft thrust of 11,500 lb at Mach 0.800 and 35,000 ft based on an NPSS model of the LEAP-1B, which includes the excess thrust required to satisfy a 300 ft/min climb rate. For the B737-8, the Turbofan-147 propulsor is sized to produce 50% of the total thrust, while for the SUSAN Electrofan, the Pod-147 and DEP-125 propulsors are sized to produce 65% of the total thrust, based on the specified thrust split, divided across two and sixteen propulsors, respectively.

Although the sizing of a propulsion system and the optimization of its performance is typically performed with at least two unique design points, e.g. TOC for sizing and cruise for performance optimization, the present paper considers only the TOC point to reduce computational cost. Performance is then evaluated at the cruise point, assuming that the difference is small for the purposes of this study.

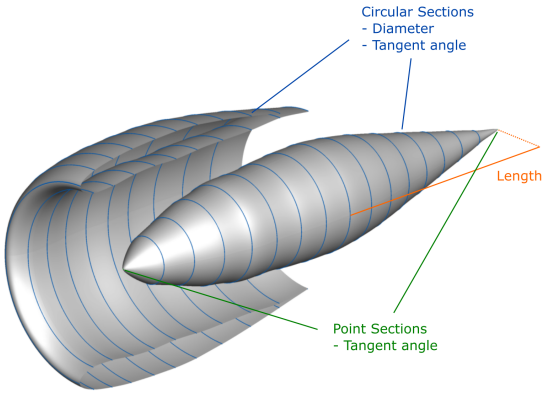
The optimization objective is to minimize shaft power while subject to constant thrust and maximum fan face Mach number constraints. Typically, the fan face Mach number of a practical design lies in the range of 0.45–0.65. In the present paper, the fan face Mach numbers of up to 0.65 are allowed. The optimization problems are defined as follows:

$$
\begin{aligned}
\text{minimize} \quad & \mathcal{P} \\
\text{w.r.t.} \quad & T, \quad \mathbf{x}_{\text{geo}} \\
\text{s.t.} \quad & T - D = 11,500 \text{ lb} \\
& M_{\text{fan}} \leq 0.65, \\
& C_{\text{geo}} = 0, \quad \mathcal{G}_{\text{geo}} \leq 0
\end{aligned}
$$

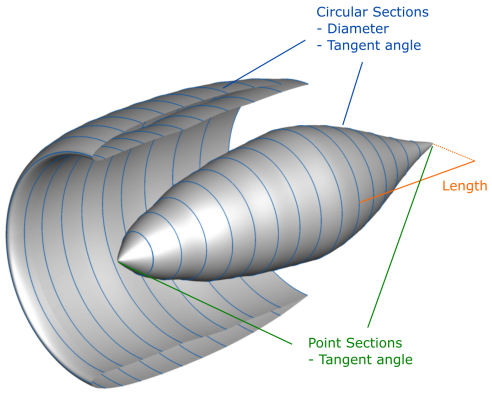
where $\mathcal{P}$ is the shaft power, T and D are the thrust and drag, respectively, $\mathbf{x}_{\text{geo}}$ is the design variable vector, which includes only geometric design variables, M_{fan} is the fan face Mach number, and C_{geo} and $\mathcal{G}_{\text{geo}}$ are the geometric equality and inequality constraints, respectively.

Figure 10 shows the geometry parameterization and control systems implemented through OpenVSP [48]. For all propulsors, the nacelle and hub are parameterized by 20 and 15 circular sections, respectively, which are controlled through diameter and tangent angle designs variables. These design variables are scalings and perturbations of the initial diameter and tangent angle values, respectively. The hub nose and aft hub tip also have point sections, which provide additional tangent angle design variables. A design variable is also included for controlling the length of the aft hub, an important parameter for capturing trades between aft hub skin-friction drag penalties and boundary layer separation. The length design variable is also a scaling factor applied to its initial value. Table 7 provides a summary of the design variables and their bounds.

With regard to geometric constraints, a minimum bound on the nacelle thickness is enforced at several chordwise stations. This prevents the thickness from reducing below 70% of its initial value in order to preserve a minimum level of



(a) Turbofan-147 and Pod-147



(b) DEP-125

Fig. 10 Wing propulsor design geometry control systems based on OpenVSP's geometry parameterization.

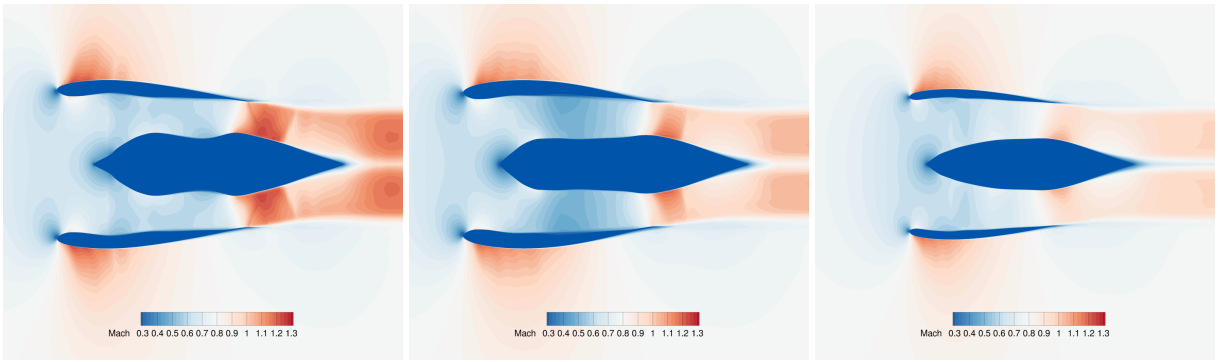
Table 7 Aeropropulsive shape optimization design variables.

Design Variable	Quantity	Lower Bound	Upper Bound
Thrust	— —	— —	— —
Turbofan-147	1	8,000 lb	12,000 lb
Pod-147	1	4,000 lb	8,000 lb
DEP-125	2	250 lb	500 lb
Diameter	35	0.8	1.2
Tangent angle	37	–45.0 deg	+45.0 deg
Length	1	0.3	1.7
Total	74–75	— —	— —

Table 8 Aeropropulsive shape optimization constraints.

Constraint	Quantity	Description
Thrust	1	Constrains the net thrust to equal the thrust required at TOC (nonlinear)
Maximum Mach at fan face	1	Constrains the fan face Mach number to not exceed a maximum bound (nonlinear)
Minimum thickness	20	Constrains the vertical separation between each pair of circular section diameters on the nacelle to be greater than or equal to 70% of its initial value (nonlinear)
LE radius	1	Constrains the LE radius to be greater than or equal to 100% of its initial value (nonlinear)
Total	20	— —

structural integrity. A minimum leading-edge radius constraint is also included to maintain a reasonable design, which in practice must consider both on- and off-design performance. A summary of the propulsor constraints is provided in Table 8.



(a) Turbofan-147 **(b) Pod-147** **(c) DEP-125**

Fig. 11 Optimized propulsor designs and centerline Mach number contours. Flow solutions are computed on the L0 grid level at M = 0.800 and 35,000 ft.

Table 9 Optimized wing propulsor aeropropulsive performance computed on the L0 grid level at M = 0.800 and 35,000 ft.

Parameter	Turbofan-147	Pod-147	DEP-125
Mach (fan face)	0.609	0.612	0.604
Mass flow rate, lb/s	551.9	501.0	89.1
Thrust 1 (gross), lb	9,770	6,550	370
Thrust 2 (gross), lb	— —	— —	340
Drag, lb	4,020	2,810	240
Thrust (net), lb	5,750	3,740	470
Fan efficiency (adiabatic)	0.935	0.950	0.961
Shaft power, hp	11,180	6,910	800

D. Wing Propulsor Optimization Results

Optimized designs for the Turbofan-147, Pod-147, and DEP-125 propulsors are obtained following similar levels of convergence to the airframe optimization problems. Figure 11 presents the optimized propulsor designs with centerline Mach number contours. These flow solutions are computed using LAVA curvilinear on the L0 grid level, with the net thrust matched with the ADFlow flow solutions. This is done to account for differences in grid topology and resolution, and is achieved by applying a Nelder-Mead optimization algorithm for determining the required actuator zone thrust inputs.

For the optimized Turbofan-147, the optimizer introduces a pointed spinner nose to achieve sufficient inlet diffusion for satisfying the maximum fan face Mach number constraint. The optimizer also introduces a concave region between the fan exit and the location of the maximum hub diameter, presumably to reduce the speed of the flow at the exit nozzle where it is close to choked. Nonetheless, only modest wave drag is experienced over the aft hub, with no boundary layer separation. Modest wave drag is also observed over the external nacelle.

The overall dimensions of the optimized Pod-147 are similar to those of the optimized Turbofan-147. This is because the optimizer chooses to increase the diameter of the Pod-147 propulsor to its maximum bound, increasing its capture area and the amount of inlet diffusion. Due to differences in the required thrust levels, the Pod-147 propulsor experiences less drag due to compressibility at the exit nozzle compared to the Turbofan-147.

Lastly, the optimized DEP-125 features relatively thin nacelles, although this is due to the already low thickness-to-chord ratios of the baseline design. Moreover, it can be seen that the low FPRs of the DEP-125 combined with its relatively high total capture area results in significantly less drag due to adverse flow features for the same total thrust requirement. Table 9 provides a summary of the optimized propulsor performance.

Table 10 Full-configuration aircraft trim state, where $F_x = 0$, $F_z = W$, and $M_y = 0$. Values are estimated based on Richardson extrapolation.

Parameter	B737-8	SUSAN-Pod	SUSAN-DEP
Angle of attack, deg	3.00	2.99	2.99
Tail incidence angle, deg	−2.33	−2.58	−2.58
Thrust, lb	12,640	15,010	13,570
F_x, lb	0.00	0.00	0.00
F_z, lb	152,480	169,130	169,130
M_y, lb-ft	0.00	0.00	0.00

VII. Full-Configuration Aircraft Performance Comparisons

In order to assess the potential benefits of the SUSAN Electrofan's DEP and BLI aft fuselage turbofan technologies, full-configuration aerodynamic and aeropropulsive performance estimates are obtained through a synthesis of the representative airframe and wing propulsor designs presented in Sections V and VI, respectively. As described in Section II, the analysis of the airframe and its wing propulsors is decoupled, with the Secant method used to determine the trim condition. Specifically, each aircraft configuration is trimmed in F_x, F_z, and M_y with respect to angle of attack, horizontal tail incidence angle, and thrust to simulate steady, level flight. This provides a means for quantifying the proposed aeropropulsive benefits of the DEP and BLI aft fuselage turbofan technologies, while accounting for differences in airframe design and aerodynamic performance between the B737-8 and the SUSAN Electrofan.

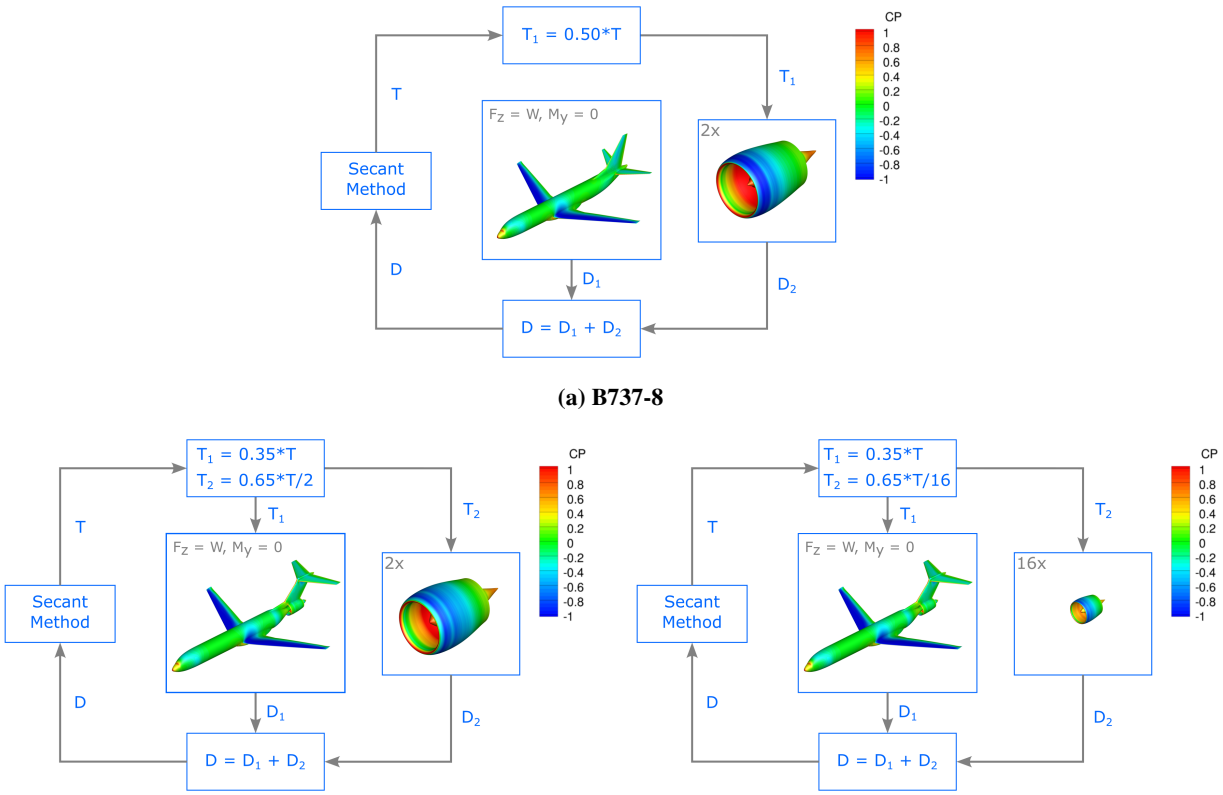
Grid convergence studies are performed for each aircraft configuration to account for differences in grid resolution between the various airframe and propulsion system components. Specifically, the grid families presented in Sections V.B and VI.B are used to estimate the grid-converged aerodynamic and aeropropulsive functionals through Richardson extrapolation, assuming a second-order rate of convergence. The aircraft configurations are also trimmed on each grid level to maintain aircraft feasibility as the grids are refined. However, since this can be computationally expensive, especially on the finest grid levels, simplifying assumptions are introduced to reduce problem complexity.

For example, thrust from all propulsors is assumed to have a negligible effect on lift and pitching moment. At cruise, negligible lift is a reasonable assumption since the angles of attack are small. With regard to pitching moment, this is a reasonable assumption for propulsion systems positioned close to z_{CG}, which is certainly the case for those of the SUSAN-DEP configuration. For the B737-8 and SUSAN-Pod configurations, this assumption results in more conservative performance estimates since accounting for the wing propulsor moments can lead to reduced trim drag from their horizontal tail. However, this is considered a higher order effect in the context of this study.

For the B737-8 configuration, these assumptions significantly reduce the number of airframe-propulsor iterations since the airframe needs to only be trimmed in F_z and M_y with respect to angle of attack and horizontal tail incidence angle. The airframe drag is then used as an input to the Turbofan-147 propulsor simulation, which is iterated with respect to the thrust input, while accounting for its own drag, to trim F_x, namely, $F_x = T_{\text{propulsors}} - D_{\text{airframe}} - D_{\text{propulsors}} = 0$.

For the SUSAN-Pod and SUSAN-DEP configurations, the airframes are also trimmed in F_z and M_y with respect to angle of attack and horizontal tail incidence with the aft fuselage turbofan powered off, based on the previously mentioned assumptions. With these state variables fixed, the airframe and wing propulsor simulations are iterated to trim F_x with respect to the aft fuselage turbofan and wing propulsor thrust inputs. Here, the assumed 35:65 thrust split between the aft fuselage turbofan and the wing propulsors is used to determine the individual thrust inputs. In addition, for the SUSAN-DEP configuration, the thrust inputs of the two actuator zones of the DEP-125 propulsors are also set to be equal to further simplify the problem. This reduces the number of thrust state variables from three to one, enabling the application of the Secant method. Note that although the simulations do not include the turbofan core, drag estimates are introduced based on free-flying core duct simulations, also with grid refinement. Figure 12 illustrates the process for determining the trim state of each aircraft configuration. The trim states are summarized in Table 10, which shows that each aircraft configuration can satisfy the force and moment balance through the three available degrees of freedom.

Table 11 presents the aerodynamic and aeropropulsive performance of the B737-8, SUSAN-Pod, and SUSAN-DEP configurations at the trim condition. Again, note that all reported values are estimated through Richardson extrapolation. It is also important to note that since the thrust values represent gross thrust, the drag values are much higher than those typically reported. This is because typical thrust-drag bookkeeping includes the internal drag of a given propulsion



(a) B737-8

(b) SUSAN-Pod

(c) SUSAN-DEP

Fig. 12 Diagrams of the iterative power balance method used to determine the trim condition for each aircraft configuration.

system in the reported thrust, a contribution that can be very high when the propulsion system is powered on. This helps to avoid ambiguity when considering aircraft configurations with high levels of PAI [19], as with the SUSAN Electrofan and its aft fuselage turbofan. Figure 13 also presents a comparison between the power on and off drag between each aircraft configuration.

Based on these results, the SUSAN-DEP configuration requires 9.6% less thrust than the SUSAN-Pod configuration, highlighting the potential aeropropulsive benefits of DEP technology. This benefit can be attributed to the higher capture area and lower FPRs of the DEP propulsors, which reduces thrust-induced drag. Indeed, the SUSAN-Pod configuration experiences a drag increment of 5,610 lb when powered on, while the SUSAN-DEP configuration only experiences 4,020 lb. This translates to 28.4% less thrust-induced drag, which comes primarily from the benefits of DEP, albeit with a modest "snowball effect" from the reduced aft fuselage turbofan thrust. In terms of thrust-induced drag per unit of gross thrust, the DEP-125 propulsors of the SUSAN-DEP configuration have a thrust-to-drag ratio of 3.9 compared to the 2.6 of the SUSAN-Pod's Pod-147 propulsors. The thrust-to-drag ratio of the aft fuselage turbofans are 2.7 and 2.8 for the SUSAN-DEP and SUSAN-Pod, respectively. Based on shaft power at the trim conditions, the SUSAN-DEP configuration provides a power savings coefficient of 4.7% relative to the SUSAN-Pod configuration.

Comparisons of the SUSAN Electrofan configurations against the B737-8 are less favorable. In terms of thrust levels, the SUSAN-Pod and SUSAN-DEP configurations require 18.7% and 7.3% more thrust than the B737-8, respectively. However, based on the airframe drag at power off conditions, the SUSAN-Pod and SUSAN-DEP configurations also experience 20.5% more drag than the B737-8. In terms of absolute values, the SUSAN-Pod configuration requires 2,370 lb more thrust at cruise relative to the B737-8, and of this difference, 1,500 lb or 63.7% comes from the difference in airframe drag. For the SUSAN-DEP configuration, 930 lb more thrust is required at cruise than the B737-8 for the same difference in airframe drag. Given that the difference in required thrust is less than the difference in airframe drag for the SUSAN-DEP configuration, this suggests that the DEP and BLI aft fuselage turbofan technologies indeed provide a drag benefit. This comes in the form of 9.4% less thrust-induced drag than the B737-8. Although, this is insufficient

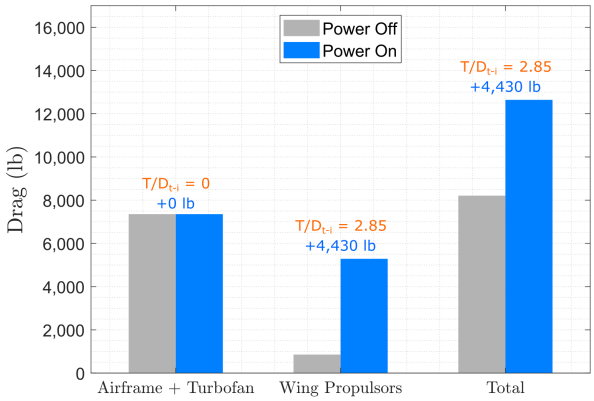
Table 11 Full-configuration aircraft aerodynamic and aeropropulsive performance at the trim condition. Values are estimated based on Richardson extrapolation.

Parameter	B737-8	SUSAN-Pod	SUSAN-DEP
Airframe + Aft Fuselage Turbofan			
Number of propulsors	0	1	1
C_L	0.556	0.589	0.589
C_D	0.0266	0.0371	0.0367
Drag, lb	7,350	10,760	10,640
Thrust (gross), lb	0	5,250	4,750
Shaft power, hp	0	5,140	4,530
Wing Propulsors			
Number of propulsors	2	2	16
C_L	0.000	0.000	0.000
C_D	0.0096	0.0073	0.0006
Drag, lb	2,640	2,120	180
Thrust (gross), lb	6,320	4,880	550
Shaft power, hp	6,740	4,930	610
Total – Full Configuration			
C_L	0.556	0.589	0.589
C_D	0.0458	0.0518	0.0468
Drag, lb	12,640	15,010	13,570
Thrust (gross), lb	12,640	15,010	13,570
Shaft power, hp	13,480	15,010	14,310
Normalized range parameter	1.000	1.133	1.189

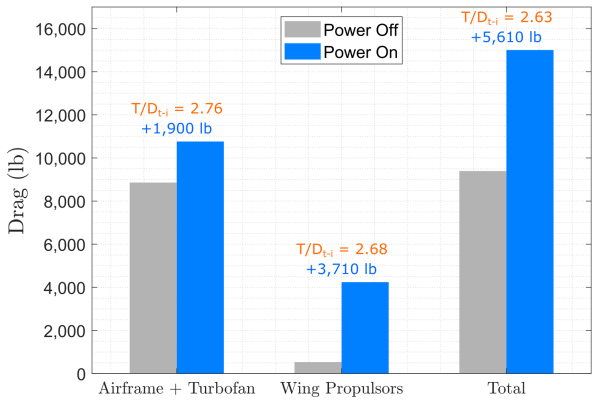
for offsetting the penalties in airframe drag, which also includes the drag of the integrated tail system and turbofan nacelle. Based on thrust-induced drag per unit of gross thrust, the B737-8 has a thrust-to-drag ratio of 2.9 compared to the 2.7 and 3.4 of the SUSAN-Pod and SUSAN-DEP configurations, respectively, accounting for all propulsion systems.

With regard to shaft power, the rate of mechanical work required by the SUSAN-Pod and SUSAN-DEP configurations to maintain the trim condition is, respectively, 11.3% and 6.1% more than that of the B737-8. This accounts for the electrical transmission losses of the SUSAN Electrofan configurations described in Section III. These results indicate that the SUSAN-Pod and SUSAN-DEP configurations do not provide a power savings coefficient benefit over the B737-8 as they are currently sized. However, as EAP technology improves, the sizing of the SUSAN Electrofan concept can be reduced with reduced EAP system weights and electrical transmission losses, opening the possibility for shaft power reductions at cruise.

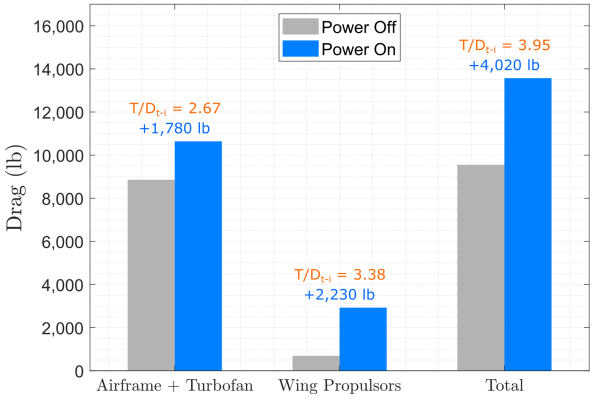
Based on Table 11, the lift-to-drag ratio of the B737-8, SUSAN-Pod, and SUSAN-DEP configurations are 12.1, 11.4, and 12.6, respectively. However, in order to compare more typical values, the thrust-drag bookkeeping is adjusted by approximating thrust as the net thrust across the fan inlet and the exit nozzle of all propulsors. This shifts the drag values to 9,870 lb, 11,370 lb, and 11,380 lb, respectively, providing lift-to-drag ratios of 15.4, 14.9, and 14.9. Since the net thrust of the propulsors do not include the drag over the aft hub, which is often also considered internal drag and is higher for the SUSAN-Pod configuration compared to the SUSAN-DEP configuration, the airframe drag of the two configurations are about the same. This is because the SUSAN-DEP configuration has higher external drag from its DEP propulsors, resulting in similar lift-to-drag ratios. Compared to the B737-8, the SUSAN-Pod and SUSAN-DEP configurations are 3.2% less aerodynamically efficient. For the SUSAN-DEP configuration, a net aerodynamic efficiency benefit may be achieved when considering the drag reductions enabled by the SUSAN Electrofan's mail-slot nacelle, as opposed to including all the external drag from the fully exposed free-flying propulsors as done in the present paper.



(a) B737-8



(b) SUSAN-Pod



(c) SUSAN-DEP

Fig. 13 Comparisons of drag with power on and power off. Drag increments are labeled in blue and measures of gross thrust per unit thrust-induced drag are labeled in orange.

Accounting for the thermal efficiency benefits of the SUSAN Electrofan's hybrid-electric propulsion system, the SUSAN-Pod and SUSAN-DEP configurations improve the range parameter by 13.3% and 18.9%, respectively, relative to the B737-8. This is entirely due to differences in TSFC at the design point of each aircraft concept. However, these TSFC values are based on conceptual propulsion system models and should be made more consistent with the aerodynamic and aeropropulsive performance estimates based on CFD analysis, for example, through modifications to the propulsive efficiency terms. Nonetheless, these results suggest that the SUSAN Electrofan has the potential provide major reductions in energy usage and emissions relative to the year 2020 technology level reference aircraft based on the Boeing 737-8, although systems analysis is still required to properly assess the impact of these metrics on mission performance.

VIII. Conclusions and Future Work

This paper presents a high-fidelity aeropropulsive assessment of the SUSAN Electrofan's DEP and BLI aft fuselage turbofan technologies through the application of computational tools for high-fidelity aerodynamic and aeropropulsive design and analysis. Representative airframe and propulsion systems are first developed in 3D for the SUSAN Electrofan and a year 2020 technology level reference aircraft based on the Boeing 737-8. These are referred to as the SUSAN-DEP and B737-8 configurations, respectively. A variant of the SUSAN Electrofan, the SUSAN-Pod configuration, is also developed with two underwing podded propulsors to serve as a non-DEP reference aircraft. The power balance method

is then used to trim the forces and moments of each aircraft configuration at cruise through decoupled simulations of the airframes and propulsion systems. This provides the means for quantifying the relative aeropropulsive performance benefits of the SUSAN Electrofan's DEP and aft fuselage turbofan systems while accounting for differences in airframe aerodynamic performance.

The airframes are developed through the application of RANS-based aerodynamic shape optimization, where the objective is to minimize drag with respect to angle of attack, wing twist, wing section shape, and horizontal tail incidence angle design variables. Constant lift and zero pitching moment constraints are included to simulate steady, level flight, and geometric constraints such as minimum wing volume and thickness are also included to reduce the impact of the aerodynamic design on non-aerodynamics disciplines. The optimized designs are capable of satisfying all optimization constraints while maintaining good transonic performance at Mach 0.785.

For the propulsion systems, the wing propulsors are modeled as simplified free-flying ducted fans developed through RANS-based aeropropulsive shape optimization. The objective is to minimize shaft power with respect to thrust and geometric design variables based on parametric models of the nacelles and hubs. Constraints include constant net thrust, maximum fan face Mach number, minimum nacelle thickness, and minimum leading-edge radius. As with the optimized airframes, the optimized propulsors satisfy all constraints and show that propulsors designed for higher FPRs result in more shaft power per unit thrust, as expected. The propulsion systems of the SUSAN Electrofan configurations also include an aft fuselage turbofan design [12], which is integrated with the fuselage and T-tail.

The angle of attack, horizontal tail incidence angle, and thrust inputs of each aircraft configuration are then driven to the trim condition, where aerodynamic and aeropropulsive analysis is performed. Results show that the SUSAN-DEP configuration requires 9.6% less thrust than the SUSAN-Pod configuration due to 28.4% less thrust-induced drag from the DEP systems. In the present paper, thrust-induced drag is measured as the drag increment from power off to power on conditions. This translates to a 4.7% power savings coefficient. Compared to the B737-8 configuration, the SUSAN-DEP configuration requires 7.3% more thrust, although much of this performance deficit comes from a 20.3% higher airframe drag based on the SUSAN Electrofan's current sizing. In terms of the ratio between gross thrust and thrust-induced drag, the SUSAN-DEP configuration has a thrust-to-drag ratio of 3.4 compared to the 2.9 of the B737-8 configuration, highlighting the aeropropulsive potential of its DEP and BLI aft fuselage turbofan technologies. Nonetheless, the SUSAN-DEP configuration currently requires 6.1% more shaft power than the B737-8 configuration when accounting for the transmission losses from its hybrid electric powertrain, assumed to be 10%.

Based on the range parameter, which considers both aerodynamic and propulsion system performance, the SUSAN-DEP is still 18.9% more efficient than the B737-8 configuration, owing primarily to its 18.6% lower TSFC. This accounts for the thermal efficiency benefits of the hybrid-electric propulsion system, which was not included in the high-fidelity aeropropulsive analysis. Although further work is required to improve the credibility of these TSFC estimates, the improvement in range parameter suggests that the SUSAN Electrofan still has the potential to reduce aviation energy usage and emissions, in part due to its DEP and BLI aft fuselage turbofan technologies. Nonetheless, systems analysis is required to better understand the impact of the range parameter on mission performance, which is reserved as future work.

Future work will also include an aeropropulsive assessment of a mail-slot nacelle concept for the DEP systems of the SUSAN Electrofan, which is expected to reduce the airframe drag penalties encountered in the present paper [9]. The aft fuselage turbofan design will also be refined through the application of aeropropulsive shape optimization, which is similarly expected to reduce the SUSAN Electrofan's aeropropulsive performance deficit.

Acknowledgments

This work is funded by the NASA Convergent Aeronautics Solutions (CAS) project, which is part of the Transformative Aeronautics Concepts Program (TACP) in the NASA Aeronautics Research Mission Directorate (ARMD). The authors gratefully acknowledge the SUSAN Electrofan team members Matthew J. Ha, Timothy P. Dever, Erik J. Stalcup, and Jonah J. Sachs-Wetstone for their technical assistance with the propulsion, electrical, power, and thermal management systems, and Ralph H. Jansen for his leadership and guidance. The authors would also like to thank Chase P. Ashby and Scott Neuhoff for internal review. Computational resources were provided by the NASA High-End Computing Capability (HECC) Program through the NASA Advanced Supercomputing (NAS) Division at Ames Research Center.

References

[1] Jansen, R., Kiris, C. C., Chau, T., Machado, L. M. G., Duensing, J. C., Mirhashemi, A., Chapman, J., French, B. D., Miller, L., Litt, J. S., Denham, C. L., Lynde, M. N., Campbell, R. L., Hiller, B. R., Blaesser, N. J., and Heersema, N., "Subsonic Single Aft Engine (SUSAN) Transport Aircraft Concept and Trade Space Exploration," *AIAA SciTech Forum and Exposition*, AIAA 2022-2179, San Diego, CA, January 2022. https://doi.org/10.2514/6.2022-2179.

[2] Cumpsty, N., and Heyes, A., *Jet Propulsion*, Cambridge University Press, 2015.

[3] Chandel, D., Reband, J. D., Hall, D. K., Balachandran, T., Xiao, J., Haran, K. S., and Greitzer, E. M., "Fan and Motor Co-Optimization for a Distributed Electric Aircraft Propulsion System," *IEEE Transactions on Transportation Electrification*, Vol. 9, No. 3, 2023, pp. 3579–3589. https://doi.org/10.1109/TTE.2022.3204202.

[4] Wick, A. T., Hooker, J. R., Hardin, C. J., and Zeune, C. H., "Integrated Aerodynamic Benefits of Distributed Propulsion," *53rd AIAA Aerospace Sciences Meeting*, AIAA 2015-1500, Kissimmee, FL, January 2015. https://doi.org/10.2514/6.2015-1500.

[5] Schmollgruber, P., Atinault, O., Cafarelli, I., Döll, C., François, C., Hermetz, J., Liaboeuf, R., Paluch, B., and Ridel, M., "Multidisciplinary of DRAGON: an ONERA Hybrid Electric Distributed Propulsion Concept," *AIAA SciTech Forum and Exposition*, AIAA 2019-1585, San Diego, CA, January 2019. https://doi.org/10.2514/6.2019-1585.

[6] Schmollgruber, P., Donjat, D., Ridel, M., Cafarelli, I., Atinault, O., François, C., and Paluch, B., "Multidisciplinary Design and Performance of the ONERA Hybrid Electric Distributed Propulsion Concept (DRAGON)," *AIAA SciTech Forum and Exposition*, AIAA 2020-0501, Orlando, FL, January 2020. https://doi.org/10.2514/6.2020-0501.

[7] Welstead, J. R., and Felder, J. L., "Conceptual Design of a Single-Aisle Turboelectric Commercial Transport with Fuselage Boundary Layer Ingestion," *54th AIAA Aerospace Sciences Meeting*, AIAA 2016-1027, San Diego, CA, January 2016. https://doi.org/10.2514/6.2016-1027.

[8] Yildirim, A., Gray, J. S., Mader, C. A., and Martins, J. R. R. A., "Boundary-Layer Ingestion Benefit for the STARC-ABL Concept," *Journal of Aircraft*, Vol. 59, No. 4, 2022, pp. 896–911. https://doi.org/10.2514/1.C036103.

[9] Machado, L. M., Chau, T., and Duensing, J. C., "Preliminary Evaluation of the Potential Benefits of a Boundary Layer Ingesting Distributed Propulsion System for the SUSAN Electrofan," *AIAA SciTech Forum and Exposition*, AIAA 2024-1327, San Diego, CA, January 2024. https://doi.org/10.2514/6.2024-1327.

[10] Machado, L. M., Chau, T., Duensing, J. C., Banchy, M. N., and Campbell, R., "Distributed Electric Propulsion System Configuration Trade Study for the SUSAN Electrofan," *AIAA SciTech Forum and Exposition*, AIAA 2025, Orlando, FL, January 2025.

[11] Anibal, J. L., and Duensing, J. C., "High-Fidelity Aeropropulsive Optimization of a Mail-Slot Distributed Electric Propulsion System for the SUSAN Electrofan," *AIAA SciTech Forum*, AIAA 2025, Orlando, FL, January 2025.

[12] Machado, L. M. G., Chau, T., Kenway, G. K. W., Duensing, J., and Kiris, C. C., "High Fidelity Computational Analysis and Optimization of the SUSAN Electrofan Concept," *AIAA SciTech Forum and Exposition*, AIAA 2022-2304, San Diego, CA, January 2022. https://doi.org/10.2514/6.2022-2304.

[13] Machado, L. M., Chau, T., Kenway, G. K., Duensing, J. C., and Kiris, C. C., "Preliminary Assessment of a Distributed Electric Propulsion System for the SUSAN Electrofan," *AIAA SciTech Forum and Exposition*, AIAA 2023-1748, National Harbor, MD, January 2023. https://doi.org/10.2514/6.2023-1748.

[14] Boeing Commercial Airplanes, *737 MAX Airplane Characteristics for Airport Planning*, Revision G, 2022. Retrieved on 1 May 2023.

[15] Gray, J. S., and Martins, J. R. R. A., "Coupled Aeropropulsive Design Optimisation of a Boundary-Layer Ingestion Propulsor," *The Aeronautical Journal*, Vol. 123, No. 1259, 2019, pp. 121–137. https://doi.org/10.1017/aer.2018.120.

[16] Chapman, J. W., Kratz, J. L., Dever, T. P., Mirhashemi, A., Stalcup, E. J., Sixel, W. R., Woodworth, A. A., and Jansen, R. H., "Update on SUSAN Concept Vehicle Power and Propulsion System," *AIAA SciTech Forum and Exposition*, AIAA 2023-1749, National Harbor, MD, January 2023. https://doi.org/10.2514/6.2023-1749.

[17] Hall, D. K., Uranga, A. C., Greitzer, E. M., Drela, M., and Sato, S., "Boundary Layer Ingestion Propulsion Benefit for Transport Aircraft," *Journal of Propulsion and Power*, Vol. 3, No. 5, 2017, pp. 1118–1129. https://doi.org/10.2514/1.B36321.

[18] Chau, T., and Duensing, J. C., "Conceptual Design of the Hybrid-Electric Subsonic Single Aft Engine (SUSAN) Electrofan Transport Aircraft," *AIAA SciTech Forum and Exposition*, AIAA 2024-1326, Orlando, FL, January 2024. https://doi.org/10.2514/6.2024-1326.

[19] Drela, M., "Power Balance in Aerodynamic Flows," *AIAA Journal*, Vol. 47, No. 7, 2009, pp. 1761–1771. https://doi.org/10.2514/1.42409.

[20] Smith, L. H. J., "Wake Ingestion Propulsion Benefit," *Journal of Propulsion and Power*, Vol. 9, No. 1, 1993, pp. 74–82. https://doi.org/10.2514/3.11487.

[21] Yildirim, A., Mader, C. A., and Martins, J. R. R. A., "A Surface Mesh Deformation Method Near Component Intersections for High-Fidelity Design Optimization," *Engineering with Computers*, Vol. 38, No. 2, 2022, pp. 1393–1425. https://doi.org/10.1007/s00366-020-01247-w.

[22] Gray, J., "Design Optimization of a Boundary Layer Ingestion Propulsor Using a Coupled Aeropropulsive Model," Ph.D. thesis, University of Michigan, 2018.

[23] Martinez-Val, R., and Perez, E., "Optimum Cruise Lift Coefficient in Initial Design of Jet Aircraft," *Journal of Aircraft*, Vol. 29, No. 4, 1992, pp. 712–714. https://doi.org/10.2514/3.46226.

[24] Torenbeek, E., "Cruise Performance and Range Prediction Reconsidered," *Progress in Aerospace Sciences*, Vol. 33, No. 5, 1997, pp. 285–321. https://doi.org/10.1016/S0376-0421(96)00007-3.

[25] Chau, T., and Zingg, D. W., "Aerodynamic Design Optimization of a Transonic Strut-Braced-Wing Regional Aircraft," *Journal of Aircraft*, Vol. 59, No. 1, 2022, pp. 253–271. https://doi.org/10.2514/1.C036389.

[26] Stalcup, E., Sachs-Wetstone, J. J., Dever, T., and Chau, T., "Thermal Management System Sizing and Analysis for the SUSAN Electrofan Aircraft," *AIAA SciTech Forum*, AIAA 2025, Orlando, FL, January 2025.

[27] Wishart, J. M., Mahavier, K., and Jansen, R. H., "Market Analysis of the Subsonic Single Aft Engine (SUSAN) Transport Aircraft Concept," *AIAA SciTech Forum*, AIAA 2023-1941, National Harbor, MD, January 2023. https://doi.org/10.2514/6.2023-1941.

[28] Culley, D. E., Kratz, J. L., and Thomas, G. L., "Turbine Electrified Energy Management (TEEM) For Enabling More Efficient Engine Designs," *AIAA Propulsion and Energy Forum*, AIAA 2018-4798, Cincinnati, OH, July 2018. https://doi.org/10.2514/6.2018-4798.

[29] Kratz, J. L., Culley, D. E., and Thomas, G. L., "Evaluation of Electrical System Requirements for Implementing Turbine Electrified Energy Management," *AIAA/IEEE Electric Aircraft Technologies Symposium (EATS)*, AIAA 2019–4502, Indianapolis, IN, August 2019. https://doi.org/10.2514/6.2019-4502.

[30] Kiris, C. C., Barad, M. F., Housman, J. A., Sozer, E., Brehm, C., and Moini-Yekta, S., "The LAVA Computational Fluid Dynamics Solver," *AIAA SciTech Forum and Exposition*, AIAA 2014-0070, National Harbor, MD, January 2014. https://doi.org/10.2514/6.2014-0070.

[31] Lowe, B. M., Ashby, C. P., Koch, J. R., Craig Penner, D. A., Housman, J. A., and Duensing, J. C., "Towards Aerodynamic Shape Optimization using an Immersed Boundary Overset Grid Method," *AIAA Aviation Forum*, AIAA 2024-4229, Las Vegas, NV, July 2024. https://doi.org/10.2514/6.2024-4229.

[32] Spalart, P. R., and Allmaras, S. R., "A One-Equation Turbulence Model for Aerodynamic Flows," *30th AIAA Aerospace Sciences Meeting and Exhibit*, AIAA 92-0439, Reno, Nevada, January 1992. https://doi.org/10.2514/6.1992-439.

[33] Shur, M. L., Strelets, M. K., Travin, A. K., and Spalart, P. R., "Turbulence Modeling in Rotating and Curved Channels: Assessing the Spalart-Shur Correction," *AIAA Journal*, Vol. 38, No. 5, 2000, pp. 784–792. https://doi.org/10.2514/2.1058.

[34] Spalart, P. R., "Strategies for Turbulence Modelling and Simulations," *International Journal of Heat and Fluid Flow*, Vol. 21, No. 3, 2000, pp. 252–263. https://doi.org/10.1016/S0142-727X(00)00007-2.

[35] Housman, J. A., Kiris, C. C., and Hafez, M. M., "Time-Derivative Preconditioning Methods for Multicomponent Flows - Part I: Riemann Problems," *Journal of Applied Mechanics*, Vol. 76, No. 2, 2009, pp. 1–13. https://doi.org/10.1115/1.3072905.

[36] Housman, J. A., Kiris, C. C., and Hafez, M. M., "Time-Derivative Preconditioning Methods for Multicomponent Flows - Part II: Two-Dimensional Applications," *Journal of Applied Mechanics*, Vol. 76, No. 3, 2009, pp. 1–12. https://doi.org/10.1115/1.3086592.

[37] Saad, Y., "A Flexible Inner-Outer Preconditioned GMRES Algorithm," *SIAM Journal on Scientific and Statistical Computing*, Vol. 14, No. 2, 1993, pp. 461–469. https://doi.org/10.1137/0914028.

[38] Stich, G. D., Fernandes, L. S., Duensing, J. C., Housman, J. A., Kenway, G. K. W., and Kiris, C. C., "Validation of Actuator Disk, Actuator Line, and Sliding Mesh Methods within the LAVA Solver," *International Conference on Computational Fluid Dynamics 11*, ICCFD, Maui, HI, July 2022.

[39] Gill, P. E., Murray, W., and Saunders, M. A., "SNOPT: An SQP Algorithm for Large-Scale Constrained Optimization," *SIAM Journal on Optimization*, Vol. 14, No. 4, 2002, pp. 979–1006. https://doi.org/10.1137/S0036144504446096.

[40] Parks, M. L., de Sturler, E., Mackey, G., Johnson, D. D., and Maiti, S., "Recycling Krylov Subspaces for Sequences of Linear Systems," *SIAM Journal on Scientific Computing*, Vol. 28, No. 5, 2006, pp. 1651–1674. https://doi.org/10.1137/040607277.

[41] Sederberg, T. W., and Parry, S. R., "Free-Form Deformation of Solid Geometric Models," *ACM SIGGRAPH Computer Graphics*, Vol. 20, No. 4, 1986, pp. 151–160. https://doi.org/10.1145/15886.15903.

[42] Hajdik, H. M., Yildirim, A., Wu, N., Brelje, B. J., Seraj, S., Mangano, M., Anibal, J. L., Jonsson, E., Adler, E. J., Mader, C. A., Kenway, G. K. W., and Martins, J. R. R. A., "pyGeo: A Geometry Package for Multidisciplinary Design Optimization," *Journal of Open Source Software*, Vol. 8, No. 87, 2023, 5319. https://doi.org/10.21105/joss.05319.

[43] Secco, N. R., Kenway, G. K. W., He, P., Mader, C. A., and Martins, J. R. R. A., "Efficient Mesh Generation and Deformation for Aerodynamic Shape Optimization," *AIAA Journal*, Vol. 59, No. 4, 2021, pp. 1151–1168. https://doi.org/10.2514/1.J059491.

[44] Mader, C. A., Kenway, G. K. W., Yildirim, A., and Martins, J. R. R. A., "ADflow: An Open-Source Computational Fluid Dynamics Solver for Aerodynamic and Multidisciplinary Optimization," *Journal of Aerospace Information Systems*, Vol. 17, No. 9, 2020, pp. 508–527. https://doi.org/10.2514/1.I010796.

[45] Pironneau, O., "On Optimum Design in Fluid Mechanics," *Journal of Fluid Mechanics*, Vol. 64, No. 1, 1974, pp. 97–110. https://doi.org/10.1017/S0022112074002023.

[46] Jameson, A., "Aerodynamic Design via Control Theory," *Journal of Scientific Computing*, Vol. 3, No. 3, 1998, pp. 223–260. https://doi.org/10.1007/BF01061285.

[47] Kenway, G. K. W., Mader, C., He, P., and Martins, J. R. R. A., "Effective Adjoint Approaches for Computational Fluid Dynamics," *Progress in Aerospace Sciences*, Vol. 168, No. 1, 2018, pp. 285–303. https://doi.org/10.1016/j.paerosci.2019.05.002.

[48] McDonald, R. A., and Gloudemans, J. R., "Open Vehicle Sketch Pad: An Open Source Parametric Geometry and Analysis Tool for Conceptual Aircraft Design," *AIAA SciTech Forum and Exposition*, AIAA 2022-0004, San Diego, CA, December 2021. https://doi.org/10.2514/6.2022-0004.

[49] Atinault, O., and Hue, D., "Design of a Vertical Tail for the CRM Configuration," Tech. rep., ONERA, June 2014. RT 1/21960 GMT/DAAP.

[50] McDonnell Douglas, "MD-80 Series Airplane Characteristics for Airport Planning," Revision 12/89, 1990.

[51] Tinoco, E. N., Brodersen, O. P., Keye, S., Laflin, K. R., Vassberg, J. C., Rider, B., Wahls, R. A., Morrison, J. H., Pomeroy, B. W., Hue, D., and Murayama, M., "Summary Data from the Seventh AIAA CFD Drag Prediction Workshop," *AIAA Aviation 2023 Forum*, AIAA 2023-3492, Kissimmee, FL, June 2023. https://doi.org/10.2514/6.2023-3492.

[52] Chau, T., Kenway, G. K. W., and Kiris, C., "Conceptual Exploration of Aircraft Configurations for the SUSAN Electrofan," *AIAA SciTech Forum and Exposition*, AIAA 2022-2181, San Diego, CA, January 2022. https://doi.org/10.2514/6.2022-2181.

[53] Zante, D. E. V., Podboy, G. G., Miller, C. J., and Thorp, S. A., "Testing and Performance Verification of a High Bypass Ratio Turbofan Rotor in an Internal Flow Component Test Facility," Tech. rep., NASA, September 2009. NASA/TM 2009-215661.

[54] Lee, B. J., and Liou, M.-F., "Conceptual Design of Propulsors for the SUSAN Electrofan Aircraft," *AIAA SciTech Forum and Exposition*, AIAA 2022, San Diego, CA, January 2022.